Evaporation-induced Cu isotope fractionation during tektite formation: Insights from laser levitation experiments

Peng Ni(倪鹏)[a,*], Catherine A. Macris[b], Emilee A. Darling[b], Anat Shahar[a]

[a]*Earth and Planets Laboratory, Carnegie Institution for Science, Washington DC 20015, USA*

[b]*Indiana University – Purdue University Indianapolis, IN 46202, USA*

This is the author's manuscript of the article published in final edited form as:

Ni, P., Macris, C. A., Darling, E. A., & Shahar, A. (2021). Evaporation-induced copper isotope fractionation: Insights from laser levitation experiments. Geochimica et Cosmochimica Acta, 298, 131–148. https://doi.org/10.1016/j.gca.2021.02.007

Abstract

As a transition metal that is moderately volatile at high temperatures, Cu shows limited isotope fractionation in mantle-derived rocks but significant enrichment in its heavier isotope (up to 12.5 per mil for $^{65}Cu/^{63}Cu$) in objects that experienced volatile loss during formation, such as tektites and lunar rocks. Previous efforts to model the Cu isotope fractionation trend from measurements of $\delta^{65}Cu$ in tektites found that the trend cannot be explained by the theoretical isotope fractionation factor (α) for free evaporation of Cu, making it necessary to experimentally study Cu isotope fractionation under conditions similar to tektite formation.

Here we present the first experimental study on Cu isotope fractionation during evaporation. Our experiments, conducted by laser-heating an aerodynamically levitated glass sphere to 1750, 2000, and 2150 ºC, show rapid loss of > 99.99% Cu from the molten glass within 60 seconds of experiment duration. The evaporation induced loss of Cu is accompanied by progressive enrichment in the heavier isotope of Cu in the residue glass, with a maximum fractionation in $\delta^{65}Cu$ of ~18‰. The empirical fractionation factor (α) calculated from our laser levitation data is 0.9960 ± 0.0002. Compared to similar experiments conducted for Zn, Cu appears to be significantly more volatile and show higher degrees of Cu isotope fractionation, consistent with observations in natural tektites.

By simultaneously comparing all available isotope fractionation data in moderately volatile elements between tektites ($^{41}K/^{39}K$, $^{114}Cd/^{112}Cd$, $^{122}Sn/^{118}Sn$, $^{66}Zn/^{64}Zn$, $^{65}Cu/^{63}Cu$, $^{208}Pb/^{204}Pb$) and the bulk silicate Moon ($^{26}Mg/^{24}Mg$, $^{30}Si/^{28}Si$, $^{65}Cu/^{63}Cu$, $^{87}Rb/^{85}Rb$, $^{7}Li/^{6}Li$, $^{71}Ga/^{69}Ga$, $^{41}K/^{39}K$, $^{66}Zn/^{64}Zn$), tektites show more extreme isotope fractionation in moderately volatile elements relative to the bulk silicate Moon, which indicates a difference in the effective degree of vapor saturation during their formation. Both tektite formation and Moon formation

occurred under conditions significantly different from the ideal situation of free-evaporation (0% vapor saturation). Laser levitation experiments show clear evidence for suppressed evaporative isotope fractionation under ambient pressure, indicating a strong vapor pressure effect on the isotope fractionation factor. Therefore, the progressively higher vapor saturation for laser levitation experiments, tektites, and the bulk silicate Moon may be related to the different vapor pressures associated with their formation.

Key words: Cu isotopes, Tektites, Laser levitation experiments, Evaporation, Moon formation

1. Introduction

Copper is a transition metal element with two stable isotopes: ^{63}Cu (69.17%) and ^{65}Cu (30.83%). It resides in the continental crust and the mantle at trace levels (28 and 30 ppm, respectively; Rudnick and Gao, 2003; McDonough and Sun, 1995) and behaves as a chalcophile and moderately siderophile element. Early measurement of Cu isotopic ratios using thermal ionization mass spectrometry did not properly correct for the instrumental isotopic fractionation of Cu and had poor analytical precision (Shields et al., 1995). Precise Cu isotope analyses were not possible until the development of plasma-source mass spectrometry and associated column purification procedures (Maréchal et al., 1999). Copper isotope measurements of mid-ocean ridge basalts (MORB), ocean island basalts (OIB), komatiites, and peridotites have yielded consistent results with an average δ^{65}Cu of 0.07 ± 0.10‰, indicating limited Cu isotopic fractionation during igneous differentiation processes (Li et al., 2009; Savage et al., 2015; Liu et al., 2015). On the other hand, Cu is also a moderately volatile element with the potential of isotopic fractionation during evaporation at high temperatures. This is evidently supported by the heavy Cu isotopic compositions for lunar basalt, lunar soil, and tektites (Fig. 1, Moynier et al., 2006; Herzog et al., 2009; Moynier et al., 2010; Rodovská et al., 2017). In particular, Cu isotopic compositions as heavy as 12.5‰ have been reported for tektites (Rodovská et al., 2017), demonstrating its potential in fingerprinting impact-related evaporation processes. Note that Cu is usually defined as a moderately volatile element based on its 50% condensation temperature (T_c) of 1037 K (Lodders, 2003); but this temperature was calculated assuming nebular conditions and cautions are needed when extrapolating to non-nebular processes.

Tektites are a type of impact ejecta formed by melting of terrestrial sediments during hypervelocity meteorite impacts. Most tektites are attributed to four known major tektite strewn

fields: North American, Central European, Ivory Coast, and Australasian tektite strewn fields. Although tektites show significant variations in composition, they are approximately felsic in term of major oxides, but relatively depleted in volatiles, including water (e.g. Koeberl, 1988; Žák et al., 2016). Furthermore, they could contain inclusions of lechatelierite (nearly pure SiO_2 glass; 99–100 wt% SiO_2) and schlieren of glass with higher SiO_2 contents than the bulk tektite (e.g. Koeberl, 1986, 1988; Glass, 1990; Howard, 2011). The presence of lechatelierite indicates that tektites reached temperatures of >1700 ºC during their formation (e.g. Barnes, 1958; Glass, 1990), consistent with an impact origin. In a more recent study, Macris et al. (2018) used interdiffusion between lechatelierite and surrounding felsic melt to estimate the thermal history of an Australasian tektite and found that tektites were heated to > 2000 ºC for several seconds to tens of seconds.

Observed volatile depletion in tektites (e.g. Koeberl, 1986; Koeberl, 1988; Žák et al., 2016), the thermal history estimates of Macris et al. (2018), the presence of lechatelierite in most tektites, and impact modeling (e.g. Melosh, 1989; Stöffler et al., 2002; Artemieva et al., 2004) indicate that tektites experienced extreme heating during their period of entrainment in the impact plume. Therefore, tektite parent melts likely underwent volatile depletion due to partial vaporization at high temperatures. In addition to the evaporative loss of Cu and the enrichment of its heavy isotopes in tektites (Moynier et al., 2010; Rodovská et al., 2017), similar observations have also been reported for other moderately volatile elements, namely Zn (Moynier et al., 2009; Rodovská et al., 2017; Jiang et al., 2019; Wimpenny et al., 2019), Sn (Creech et al., 2019), Cd (Wombacher et al., 2003), and Pb (Ackerman et al., 2020).

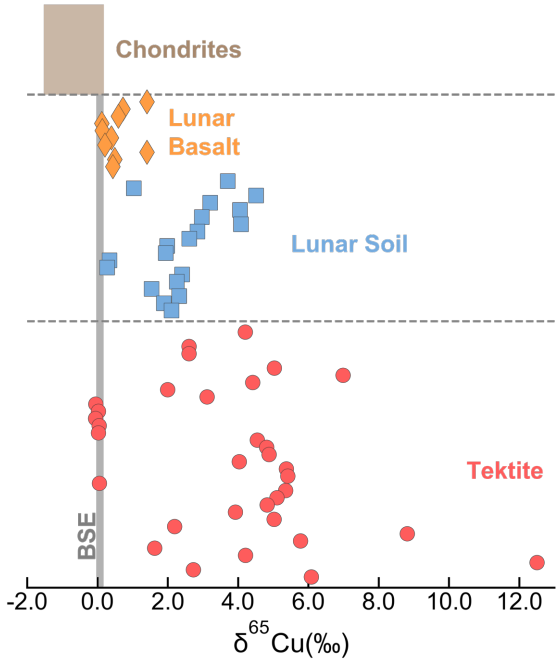

Figure 1. Compiled Cu isotope data for chondrites, lunar basalt, lunar soil, and tektites (Moynier et al., 2006; Herzog et al., 2009; Moynier et al., 2010; Savage et al., 2015; Rodovská et al., 2017). Bulk Silicate Earth Cu isotope composition of 0.07 ± 0.10‰ is from Savage et al., (2015). Analytical errors of the measurements are smaller than the symbol size.

Despite the robust literature on tektites, there are still fundamental outstanding questions regarding the role of volatilization in their chemical and isotopic fractionation. For example, Cu is usually expected to be more volatile than Zn based on their half condensation temperatures in the solar nebular (1037K and 726 K, respectively Lodders, 2003). However, relatively large magnitudes of Cu isotope fractionation are measured in natural tektites (up to 12.5‰ Rodovská et al., 2017) compared to more limited magnitudes for Zn (3.65‰ in the same sample, Rodovská et al., 2017), which is contrary to the expectation. To explain why Cu is isotopically more fractionated than the more volatile Zn in the same tektites, Moynier et al. (2010) proposed that isotopic fraction in tektites is controlled by a diffusion-limited regime, in which evaporation of Cu and Zn is dominated by their diffusivities in silicate melts. This was subsequently supported

by experiments showing significantly higher diffusivity of Cu than Zn in silicate melts (by 4 orders of magnitude at 1150 ºC, Ni et al., 2017).

On the other hand, recent evaporation experiments have advanced our understanding on the behavior of moderately volatile elements in silicate melts as a function of temperature and oxygen fugacity (Norris and Wood, 2017; Sossi et al., 2019). Both studies demonstrated that the volatility sequence relevant to geological processes could depart significantly from that predicted based on the 50% condensation temperatures calculated for solar nebular conditions (Lodders, 2003). In Norris and Wood (2017), for example, Cu was shown to be more volatile than Zn at $\log f(O_2)$ = -11 to -7 under 1 bar and 1300 ºC. More recently, Jiang et al. (2019) conducted thermodynamic modeling on fractional evaporation of Chinese loess when producing the Hainan tektites, and found a volatility sequence of Cu > Zn >> K at 1500 K that best matches the observed depletion factors in tektites for these elements. The same study reported *in situ* Zn, Cu, and K concentration measurements, and Zn and K isotope ratios, from a cross section of a Hainan splashform tektite (9 cm × 3.5 cm). These data do not show any systematic zoning or gradients from the center to the edge of the sample, which disfavors the idea of diffusion limited fractionation. Overall, it is not fully understood yet whether the larger isotopic fractionation in Cu versus Zn is due to a diffusion-limited regime, more volatile behavior of Cu during tektite formation, or some combination of these factors.

In addition to the relatively larger isotopic fractionation in Cu than Zn, previous studies also found it difficult to explain the isotope fractionation trend using theoretical isotope fractionation factors for free-evaporation (Moynier et al., 2009; Moynier et al., 2010; Rodovská et al., 2017). Wimpenny et al. (2019) conducted evaporation experiments using rhyolitic and arkosic soils that yielded a fractionation factor (α) of 0.9988 for Zn, broadly matching the

estimated α values between 0.9988 and 0.9997 for australite tektites. Their experiments demonstrated suppressed fractionation factors for moderately volatile elements during tektite formation, consistent with previous experiments that found K isotope fractionation factors to be pressure-dependent (Yu et al., 2003). Despite recent efforts in understanding Zn isotope fractionation for tektites (Wimpenny et al. 2019), no similar studies have been done yet to quantitatively understand Cu isotope fractionation in the same process. In this study, we conducted laser levitation experiments on Cu-bearing silicate glasses to simulate tektite formation and evolution in the impact plume. Changes in Cu concentration and isotope fractionation have been measured in the experimental products to understand the behavior of Cu and its isotopes during impact-related evaporation processes. Our results are then combined with similar experiments on Zn in Wimpenny et al. (2019), natural tektite data, and lunar rock data to provide a general framework on how moderately volatile elements behave during evaporation under conditions related to tektite and Moon formation.

2. Methods

2.1. Laser levitation experiments

The starting material for our experiments was an aliquot of synthesized Cu-bearing basaltic glass (Et1Cu) previously used for diffusion experiments of Ni and Zhang (2016). The glass contains 46.18 wt% SiO_2, 1.63 wt% TiO_2, 18.17 wt% Al_2O_3, 10.67 wt% FeO_t, 5.84 wt% MgO, 10.69 wt% CaO, 4.45 wt% Na_2O, 1.90 wt% K_2O, and 1174 ± 121 ppm Cu based on electron microprobe analyses (Ni and Zhang, 2016). This initial glass (Et1Cu) was fused at 1300 ºC for 3 h using a graphite crucible under a constant N_2 flow and contained low H_2O concentration (~10 ppm, Ni and Zhang, 2016). Silicate glasses synthesized following this

147 procedure were found to be fairly reducing, with a Fe^{3+}/Fe_{tot} ratio of ~0.04 (Guo and Zhang,
148 2018) and dissolved Cu being monovalent (Ni and Zhang, 2016). Vaporization experiments were
149 performed in the High-Temperature Conical Nozzle Levitation (HT-CNL) System (this
150 apparatus is sometimes also called an aerodynamic levitation laser furnace) at Indiana University
151 – Purdue University Indianapolis (IUPUI). The apparatus components and mode of operation are
152 shown schematically in Fig. 2. In this technique, a spherical sample, ~0.5 to 3 mm in diameter, is
153 levitated by a gas (or gas mixture) issuing from a conical nozzle while being heated with a 400
154 W CO_2 laser (10 µm, IR). Sample temperature is measured by a pyrometer while being
155 controlled by adjusting the laser power to achieve the desired experimental temperature-time (*T*-
156 *t*) conditions. Maximum temperatures achievable by the apparatus are ≥ 3000 K. Heating and
157 levitation take place in a controlled-atmosphere chamber. The use of containerless processing by
158 aerodynamic levitation and laser heating avoids common problems encountered in evaporation
159 experiments using traditional approaches, such as sample reaction with a container or contact
160 wire (e.g. Ni crucible in Norris and Wood, 2017; and Pt wire in Sossi et al., 2019).

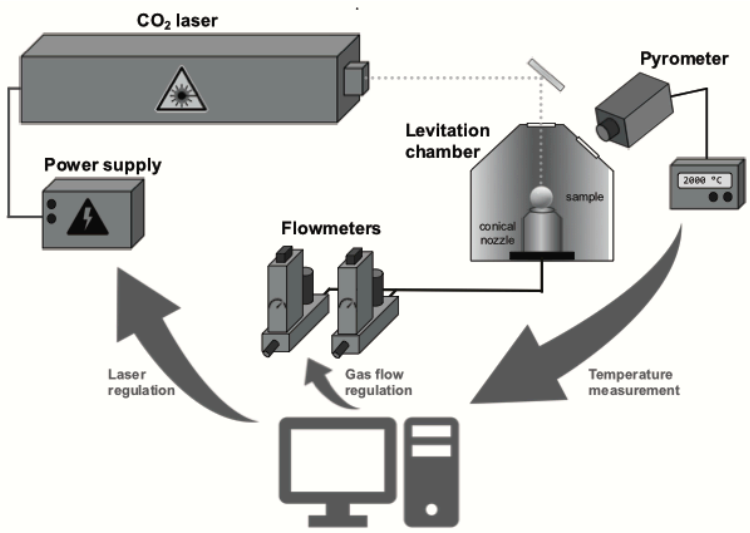

161

162 **Figure 2.** Schematic representation of the High Temperature Conical Nozzle Levitation (HT-
163 CNL) system (also known as an aerodynamic levitation laser furnace) at IUPUI showing the

main components and mode of operation of the apparatus. Inside of an atmospherically-controlled levitation chamber, a small spherical sample (~0.5–3 mm) is freely floated on top of a vertical gas stream issuing from a conical nozzle while being heated from above with a 400 W CO_2 laser. Temperature is measured by pyrometry while laser power and gas flow as well as gas mixing are controlled by a LabVIEW program. Parts of the figure are modified after Landron et al. (2000). The components in the figure are not depicted to scale.

Pack et al. (2010) described examples of Earth and planetary science applications using aerodynamic levitation combined with laser heating, including alkali evaporation during chondrule melting and *in situ* reduction of silicate melts. Macris et al. (2018) showed that this type of instrument can be used to successfully simulate compositions and textures of terrestrial impact glasses and induce partial vaporization of levitated melts. Experimental procedures in this study followed those outlined in Macris et al. (2018) and are briefly described below. Prior to levitation, ~10 mg aliquots of the Cu-bearing starting glass (Et1Cu) were fused into spheres suitable for levitation in a water-cooled oxygen-free hearth plate by defocused laser heating. This method of sample preparation results in negligible sample contamination and material loss (Weber et al., 1996), including in Fe-bearing systems (Alderman et al., 2017a, b). One fused glass sphere that was not subsequently used in a levitation heating experiment was analyzed as a control to verify that the fusion process does not result in evaporative loss of Cu or isotope fractionation (Cu 1.15, Table 1). After being carefully weighed and measured for their diameters, the fused glass spheres were heated to 1750, 2000, and 2150 ºC for 4 to 120 s while levitated in 99.999% Ar, and then quenched to glass by cutting power to the laser.

Since the duration of our laser-levitation experiments could be as short as 4 s, the following correction is conducted to account for the amount of time spent on heating up and quenching the glass spheres:

$$t_c = \frac{\int \exp\left(\frac{\Delta H}{-RT}\right)/\sqrt{T} \cdot dt}{\exp\left(\frac{\Delta H}{-RT_0}\right)/\sqrt{T_0}}, \quad (1)$$

in which t_c is the corrected duration at the target temperature T_0; T is the recorded temperature at a given time (t), and ΔH is the enthalpy for the Cu evaporation reaction from Sossi et al. (2019). A detailed deduction for eq. (1) is provided in Appendix B. This correction typically adds 3 s to 4 s to the recorded duration.

2.2. Cu isotope analyses

2.2.1 Ion-exchange chromatography

Following the laser-levitation experiments, each quenched glass sphere was weighed and measured for its diameter again, before being dissolved in a mixture of concentrated HF-HCl (2:1) in a Teflon beaker. The Teflon beaker was placed on a hot plate for at least two days to achieve complete dissolution. After dissolution, the sample was dried down and taken up in 1 ml concentrated HCl, and then dried down again to remove F^- in the sample. The process is repeated twice to minimize F^- residue in the sample. The chemical purification procedure in this study is modified from the long column method in Sossi et al. (2015). In-house custom-made quartz glass columns with a diameter of 0.4 cm were loaded with ~7.5 cm AG1-X8 (200-400 mesh) BioRad resin for Cu separation. To purify Cu from matrix elements in the silicate glass, the sample was loaded onto the column in 1 ml 8M HCl + 0.001% H_2O_2. As shown in the elution curve based on BHVO-2 (Supplementary Fig.1), most matrix elements can be eluted in the first 7 ml 8M HCl + 0.001% H_2O_2, leaving Cu, Co, Fe, and Zn adsorbed on the resin. Copper was then collected by eluting another 9 ml 8M HCl + 0.001% H_2O_2 through the column. Subsequently, remaining Co, Fe, and Zn left on the column was removed by adding 5 ml 1M HNO_3. The Cu purification procedure was repeated again to ensure complete separation of Cu from matrix elements. After the column procedures, the Cu fraction was evaporated to dryness, re-dissolved in a few drops of

concentrated HNO_3 and dried down twice to drive away Cl^-, before being dissolved in 0.4M HNO_3 for mass spectrometer analyses.

After column chemistry, the amount of Cu collected for each experimental sample was measured by comparing its peak intensity on the mass spectrometer to a solution standard with known Cu concentration. The Cu concentration in each experimental sample was subsequently calculated by comparing the amount of collected Cu with the total weight of the experimental product. The detection limit for Cu concentration is obtained by dividing the procedural blank (0.5 ng) by the weight of the experimental sample, and was ~0.03 ppm. The error for the calculated Cu concentration is a complex function of the Cu column yield, the dilution processes, and the peak intensity measurements on the mass spectrometer, and is estimated to be within 10% relative. The experimental samples selected for Cu isotope analyses contained 51 ng to 22.2 µg Cu, significantly higher than the total procedural blank of 0.5 ng. The recovery rate of the column procedure was regularly monitored to be > 99% by: 1) running a known amount of Cu isotope standard (ERM-AE633) through the column and measuring the yield; and 2) checking for the absence/presence of Cu in the aliquots that bracket the Cu peak in the column procedure.

2.2.2 Mass spectrometry analyses

Copper isotopic analyses were conducted in low-resolution mode on the Nu Plasma II at the Earth and Planets Laboratory, Carnegie Institution for Science. Samples and standards were typically diluted to ~100 ppb Cu in 0.4 M HNO_3 solutions for analyses, except for Cu 1.1 and Cu 1.7, which were diluted to ~10 and ~40 ppb, respectively, because of their low Cu contents. With a sensitivity of ~2.5 V/ 100 ppb for ^{63}Cu, even analyses using ~10 ppb Cu solutions yielded sufficient precision (2 s.e. = 0.09‰, n = 11) for our evaporation experiments (Supplementary

Fig. 2), in which Cu isotopes fractionate by several per mil or higher. Corrections for instrumental mass bias were made by sample-standard bracketing with the respective signal levels matched to better than 5% between sample and standard. Each sample was measured 4 to 8 times and each measurement consisted of 20 cycles with 4 s integrations. The bracketing standard used in the study was ERM-AE633, a new reference material with an isotopic composition 0.01‰ lighter than the international Cu standard NIST SRM 976, which is no longer commercially available. To be consistent with previous Cu isotope studies, all our results are reported relative to NIST SRM 976 after correcting a -0.01‰ difference between ERM-AE633 and NIST SRM 976 (Moeller et al., 2012):

$$\delta^{65}\mathrm{Cu} = \left[\left(^{65}\mathrm{Cu}/^{63}\mathrm{Cu}\right)_{\mathrm{Sample}}/\left(^{65}\mathrm{Cu}/^{63}\mathrm{Cu}\right)_{\mathrm{SRM976}} - 1\right] \times 1000$$

$$= \left[\left(^{65}\mathrm{Cu}/^{63}\mathrm{Cu}\right)_{\mathrm{Sample}}/\left(^{65}\mathrm{Cu}/^{63}\mathrm{Cu}\right)_{\mathrm{AE633}} - 1\right] \times 1000 + 0.01‰ \qquad (2)$$

An in-house Cu concentration standard was analyzed in each session as a quality-control procedure. Two geological standards, BIR-1 and BHVO-2, were also analyzed as a comparison with literature values. Our analyses yielded a δ^{65}Cu of 0.08 ± 0.05‰ (n=26, 2 s.d.) for BHVO-2 and -0.07 ± 0.04‰ (n=8, 2 s.d.) for BIR-1, broadly consistent with literature values reported for both geological standards (0.06 ± 0.01 to 0.19 ± 0.05‰ for BHVO-2; -0.03 ± 0.06 to 0.09 ± 0.01‰ for BIR-1; Moynier et al., 2010; Moeller et al., 2012; Liu et al., 2014; Savage et al., 2015; Liu et al., 2015; Chen et al., 2016).

3. Results

Results of all 17 experiments conducted in this study are summarized in Table 1. Most of the experiments (15 out of 17) were conducted at two temperatures (2000 and 2150 ºC) to study the evaporative loss of Cu as a function of time, as well as the associated Cu isotope

fractionation. One experiment was performed at 1750 ºC to check for the temperature effect at a lower temperature. Experiment Cu 1.15 did not undergo any laser heating and was used as a control sample to examine potential Cu loss and Cu isotope fractionation during the fusion process (starting glass sphere preparation step; see Section 2.1). Analyses of the powdered starting glass, Et1Cu, yielded 1185 ppm Cu in the glass, with an initial δ^{65}Cu = 3.46 ± 0.02‰ (Table 1). The control sample, Cu 1.15, which only experienced fusion by defocused laser heating in a water-cooled oxygen-free hearth plate to form a glass sphere, demonstrates limited loss of Cu compared with the starting glass powder (C_{Cu} = 1129 ppm Cu; δ^{65}Cu = 3.17‰, Table 1) and provides a reasonable constraint on the initial Cu concentration and Cu isotope composition for our experiments.

3.1 Evaporative loss during extreme heating

During the laser levitation experiments, basaltic glass spheres were heated to temperatures ranging from 1750 to 2150 ºC and experienced extensive evaporation, as evidenced by their loss in total mass and rapid decrease in Cu concentration (Table 1). According to the Hertz-Knudsen equation, the evaporative flux for a particular species through the surface of a melt sphere over a given time interval is:

$$\frac{dn}{dt} = -4\pi r^2 \frac{\alpha_{ec}(P_{sat}-P)}{\sqrt{2\pi RMT}}, \quad (3)$$

where dn/dt is the net evaporative flux; r is the radius of the sphere; P_{sat} is the equilibrium partial pressure; P is the partial pressure at the surface; M is the molar mass; R is the gas constant; T is the temperature; and α_{ec} is the dimensionless evaporation/condensation coefficient ($0 < \alpha_{ec} < 1$). Solving eq. (3) (Appendix A; also see Sossi et al., 2019) yields:

$$ln\frac{C}{C_0} = -kt, \quad (4)$$

where C/C_0 is the concentration change relative to its initial value, t is time, and k is a constant. Equation (4) is a simplified form of eq. (A10) and it demonstrates that evaporative loss of a component depends on time exponentially.

Plotting $-\ln(C_{Cu}/C_{Cu,0})$ versus time in Fig. 3a shows that the loss of Cu is approximately logarithmic, consistent with evaporative loss as predicted by eq. (4) and previous evaporation experiments (e.g. Yu et al., 2003; Wimpenny et al., 2019; Sossi et al., 2019). Overall, Cu concentration in the melt sphere decreases by four orders of magnitude within one minute, rapidly reaching the detection limit of ~ 0.03 ppm for Cu. Among the three sets of experiments at 1750, 2000, and 2150 ºC, the best trend in Fig. 3a is obtained for experiments at 2000 ºC. After excluding the longest-duration experiment with a Cu concentration at the detection limit, the rest of the experiments at 2000 ºC can be fit with a linear function, which yields $-\ln(C_{Cu}/C_{Cu,0}) = (0.16 \pm 0.01)t$, with an R^2 of 0.992 (Fig. 3a). On the other hand, experiments at 1750 and 2150 ºC show temperature dependence of the evaporation induced fractionation, as expected from Eq. (A10). The only experiment at 1750 ºC falls below the trend for 2000 ºC experiments, while experiments at 2150 ºC with durations of < 60 s are generally above the trend, indicating a positive temperature effect on evaporation (Fig. 3a). The four experiments at 2150 ºC with durations of < 60 s do not form a linear trend, making it difficult to quantify the temperature effect. Although eq. (1) is employed in this study to correct the experimental duration for heating and quench times, the amount of time needed for the sample to achieve evenly thermal distribution is not accounted for and may introduce random errors to the experimental duration, especially for those with short durations and at higher temperatures.

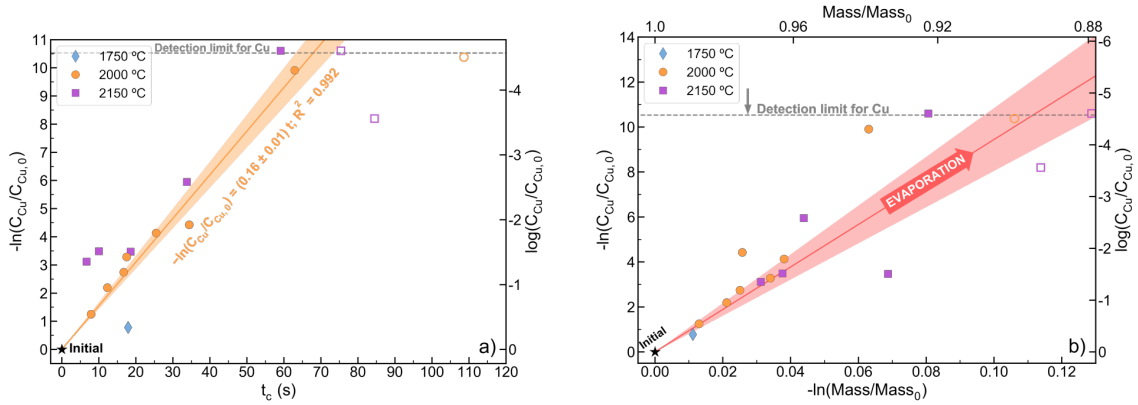

Figure 3. Evaporative loss of Cu and the total mass in our laser levitation experiments. a) the fraction of Cu loss (-ln($C_{Cu}/C_{Cu,0}$)) plotted versus the corrected duration (t_c) shows good linear correlation, which is characteristic for evaporation processes; b) the fraction of Cu loss versus the fraction of total mass loss. Experiments with durations > 60 s are expected to reach the detection limit for Cu concentration and are plotted in open symbols. In a), after excluding the longest-duration experiment (Cu 1.1, marked in open circle), a linear fitting of all other experiments at 2000 ºC is shown and the shadowed region represents 2σ error.

In Fig. 3b, the change in Cu concentration of our experiments is plotted versus the total mass loss in natural logarithm scale for comparison. The maximum mass loss achieved in our experiments is ~11 to 12 wt% (Table 1), two orders of magnitude higher than what could be contributed by the loss of Cu (0.11 wt%) from the initial samples. Because the starting basaltic glass was synthesized in a one-atmosphere furnace with a N_2 flow, it contains only ~10 ppm H_2O based on FTIR measurements (Ni and Zhang, 2016). Therefore, the measured mass losses in our experiments are more likely due to evaporative loss of Na_2O (4.45 wt%), K_2O (1.90 wt%), and FeO (10.67 wt%), as shown in similar experiments by Wimpenny et al. (2019). Plotting -ln($C_{Cu}/C_{Cu,0}$) versus -ln(Mass/Mass$_0$) in Fig. 3b shows a broadly positive correlation between the two parameters, indicating that the total mass loss is also dominated by evaporation. The correlation is not perfectly linear, probably because the total mass loss is a complex function of evaporation loss for all vaporizing species, and does not necessarily follow the exponential function in eq. (4). Nonetheless, experiments at 1750, 2000, and 2150 ºC fall broadly on a single

trend in Fig. 3b, indicating that temperature affects Cu evaporation loss and total mass loss to a similar extent, and the effect is more apparent when plotting them versus each other.

3.2 Copper isotope fractionation during evaporation

Copper isotope compositions of the glass spheres after heating show a consistent enrichment in the heavier isotope relative to the starting glass, and the magnitude of isotope fractionation correlates positively with the heating temperature and duration. The largest extent of Cu isotope fractionation measured in our experiments is about 18‰ (Cu 1.2), even higher than the maximum δ^{65}Cu of 12.5‰ observed in tektites (Rodovská et al., 2017).

Isotope fractionation of Cu during evaporation can be related to its concentration change through the Rayleigh relationship:

$$\frac{R}{R_0} = F^{\alpha-1} = \left(\frac{C}{C_0}\right)^{\alpha-1}, \quad (5)$$

where R is the ^{65}Cu/^{63}Cu ratio in a sample after experiment, R_0 is its initial ^{65}Cu/^{63}Cu ratio, F is the fraction of Cu that remains after the experiment and is equal to the ratio of Cu concentration in the sample (C_{Cu}) over its initial Cu concentration ($C_{Cu,0}$), and α is the Cu isotope fractionation factor. Taking the natural logarithm of both sides of eq. (5), we obtain:

$$\ln (R/R_0) = (\alpha - 1) lnF = (\alpha - 1) \ln (C/C_0). \quad (6)$$

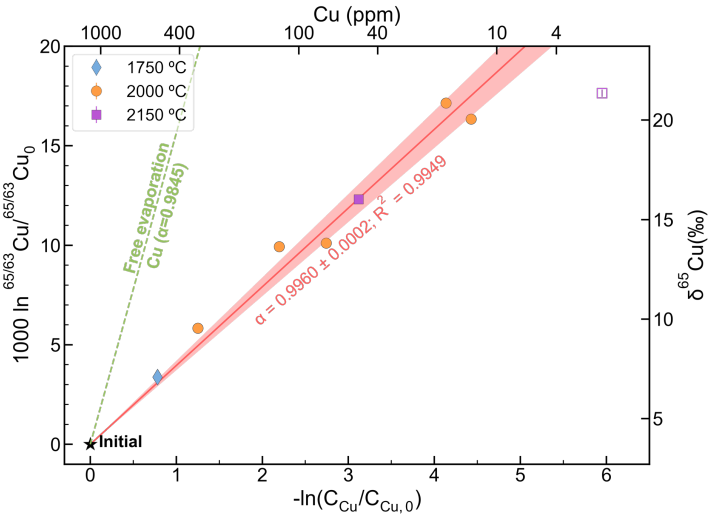

Figure 4. Copper isotope fractionation ($1000\ln{}^{65/63}Cu/{}^{65/63}Cu_0$) as a function of Cu evaporative loss ($-\ln C_{Cu}/C_{Cu,0}$) for the laser levitation experiments. Here ${}^{65/63}Cu$ and ${}^{65/63}Cu_0$ are the ${}^{65}Cu/{}^{63}Cu$ ratios in the evaporated samples and in the initial glasses, respectively. A linear fitting of the data, after excluding one outlier (open square), is plotted as the red straight line. The shadowed area represents 2σ uncertainty on the slope. The slope of the fitted line represents 1000(1-α) and gives an $\alpha = 0.9960 \pm 0.0002$ (2σ) for Cu. Expected isotope fractionation for free evaporation of Cu is plotted in green dashed curve for comparison.

Therefore, by plotting $\ln(R/R_0)$ versus $-\ln(C/C_0)$, a straight line with a slope of $1-\alpha$ is obtained if the evaporation process obeys the Rayleigh fractionation law. As shown in Fig. 4, for those samples which we analyzed for Cu isotopes, most fall onto a linear trend, which propagates from starting material composition. Fitting the trend with a linear function yields a well constrained Cu isotope fractionation factor of 0.9960 ± 0.0002 (Fig. 4). In comparison, the theoretical isotope fractionation factor for free evaporation of Cu is 0.9845. The only experiment that departs from the general trend is the experiment Cu 1.2, which has the lowest Cu concentration (2.7 ppm) among all samples measured for $\delta^{65}Cu$ in our study. Because of the low Cu content in Cu 1.2 (51 ng total Cu), it is more easily affected by re-condensation of Cu on the bead surface after quench. Only several nanograms of isotopically light Cu condensates on the bead surface is sufficient in explaining its departure from the Rayleigh fractionation curve (Fig.

4). The same process can be used to explain the relatively high Cu concentration of 0.31 ppm in Cu 1.5 (~5 ng total Cu), which has the longest heating duration of 120 s at 2150 ºC and is expected to contain < 0.03 ppm Cu. Nonetheless, four of the laser levitation experiments yielded Cu concentrations close to the detection limit of 0.03 ppm, indicating that this potential surface condensation only occurs occasionally. The level of contamination has a more profound effect on experiments with low Cu concentration (i.e. < 10 ppm), but is marginal to most of the experiments reported in this study (Table 1).

4. Discussion

4.1 Comparing to previous laser levitation experiments for Zn

4.1.1 Evaporative loss of Cu and Zn in laser levitation experiments

In this section, our experiments are compared with previous laser levitation experiments reported by Wimpenny et al. (2019) to understand the evaporation-induced depletion of both Cu and Zn. In Wimpenny et al. (2019), two sets of experiments were conducted using an arkosic soil and a rhyolitic soil, respectively. The arkosic soil, collected from the Trinity nuclear test site, consists of alkali feldspar, sodic plagioclase, quartz, and limestone fragments; while the rhyolitic soil consists of K-feldspar, quartz, plagioclase, and glassy groundmass. As mentioned earlier, the set of experiments conducted using the arkosic soil in Wimpenny et al. (2019) indicates a labile Zn reservoir that quickly evaporated without causing any Zn isotope fractionation. Such a Zn reservoir complicates the calculation of Zn depletion factors. Therefore, experiments using the arkosic soil from Wimpenny et al. (2019) are excluded in our discussion for simplification, as they are not analogous to the vaporization processes in our experiments. Nevertheless, after correcting for the effect of quantitative Zn loss, these experiments fall on the same trend as the

rhyolitic soil experiments. To avoid complications caused by the experimental temperature and melt sphere diameter, only experiments with the same temperature (2000 ºC) and similar sample diameters (~2mm) from this study and from Wimpenny et al. (2019) were selected for comparison. A correction of 3.5 s was added to the reported experimental durations from Wimpenny et al. (2019) to account for the heating and quench part of the experiments, based on the corrections done in this study (3 to 4 s).

In Fig. 5, evaporative loss of Zn and Cu as a function of time and the related isotope fractionation are compared for laser levitation experiments at 2000 ºC. As can be seen in Fig. 5a, Cu exhibits significantly higher volatility compared to Zn. Within an experimental duration of 120 s, Zn concentration in the rhyolitic soil from experiments by Wimpenny et al. (2019) decreased only by 33%, while Cu concentration in our basaltic glass experiments decreased by over four orders of magnitude in 60 s. Fitting the depletion trends for Cu and Zn in Fig. 5a yields:

$$-ln\frac{C_{\mathrm{Cu}}}{C_{\mathrm{Cu},0}} = (0.16 \pm 0.01)t_c, R^2 = 0.992, \quad (7)$$

and

$$-ln\frac{C_{\mathrm{Zn}}}{C_{\mathrm{Zn},0}} = (0.0023 \pm 0.00028)t_c, R^2 = 0.575. \quad (8)$$

Assuming the loss of Cu and Zn is purely controlled by evaporation, solving the Hertz-Knudsen equation (eq. 3) (Appendix A) gives:

$$ln\frac{C_i}{C_{i,0}} = -\frac{3\alpha_{ec}(1-s)\gamma_i K}{r\rho f(O_2)^{\frac{n}{4}}}\frac{M_{\mathrm{melt}}}{\sqrt{M_i}}\sqrt{\frac{1}{2\pi RT}}t, \quad (9)$$

where C_i is the concentration of Cu or Zn at a given time (t), $C_{i,0}$ is their initial concentration, M_i is their molar mass, M_{melt} is the molar mass of the melt, α_{ec} is the dimensionless evaporation/condensation coefficient ($0 < \alpha_{ec} < 1$), s is the saturation index defined as s =

$P_i/P_{i,sat}$ (eq. A3), γ_i is the activity coefficient of Cu or Zn in the melt, K is the equilibrium constant, r is the radius of the melt sphere, ρ is the density of the melt, $f(O_2)$ is the oxygen fugacity, n is the number of electrons transferred in the evaporation reaction, R is the gas constant, T is the temperature, and t is the experiment duration.

Defining the experimental factor, k_{exp}, as $k_{exp} = \frac{3M_{melt}}{r\rho\sqrt{2\pi RT}}$ and the elemental factor, k_{ele}, as $k_{ele} = \frac{\alpha_{ec}\gamma_i K}{\sqrt{M_i}}$, eq. (9) can be rewritten as:

$$ln\frac{C_i}{C_{i,0}} = -(1-s)\cdot f(O_2)^{-\frac{n}{4}}\cdot k_{exp}k_{ele}t. \quad (10)$$

The experimental factor (k_{exp}) consists of parameters in eq. (9) that are related to the experiment design, including the radius of the melt sphere (r), the experiment temperature (T), and the density (ρ) and molar mass (M_{melt}) of the melt. For the Zn and Cu experiments compared in Fig. 5, the differences in the above parameters are relatively small (< 20%). Therefore, k_{exp} can be excluded as a major contribution to the observed volatility difference between Cu and Zn in Fig. 5a. The saturation index (s), as will be shown later based on the isotope data, is not different enough in laser levitation experiments to cause such a large difference in evaporation rate. The elemental factor (k_{ele}), which consists of parameters in eq. (9) that are specific to the element, could differ significantly between Zn and Cu. This is especially true for the activity coefficient (γ_i) and the equilibrium constant (K) of the evaporation reaction, which could differ by orders of magnitude as shown in Jiang et al. (2019) and Sossi et al. (2019).

Oxygen fugacity also plays an important role in affecting the evaporation rate of Cu and Zn. This is because the valance state change is different for Cu and Zn during evaporation. Zinc only exists as Zn^{2+} in natural silicate melts because it has only one possible oxidization state. On the other hand, Cu is almost always Cu^{+} in natural silicate melts, as indicated by studies on Cu

solubility and diffusivity in silicate melts (e.g. Ripley and Brophy, 1995; Holzheid and Lodders, 2001; Liu et al., 2015; Ni et al., 2017). The monovalent state of Cu in silicate melts applies to a wide range of silicate composition and oxygen fugacity, which means the role of Cu^{2+} can be ignored when discussing Cu evaporation in silicate melts.

According to the experiments in Sossi et al. (2019), both Cu and Zn evaporate to the gaseous phase in the form of native metal over a wide range of oxygen fugacity, consistent with evaporation reactions of $CuO_{0.5}(l) = Cu(g) + 1/4O_2$ and $ZnO(l) = Zn(g) + 1/2O_2$. Substituting n=1 for Cu (Cu^+ to Cu^0) and n=2 for Zn (Zn^{2+} to Zn^0) into eq. (11) shows that Cu evaporation depends on $f(O_2)^{-\frac{1}{4}}$ while Zn evaporation depends on $f(O_2)^{-\frac{1}{2}}$, indicating a stronger dependence of Zn volatility on oxygen fugacity. Since both sets of experiments used high-purity Ar as the levitation gas medium, the oxygen fugacity is expected to be similar and was unlikely a dominating factor in causing the observed volatility difference between Cu and Zn. Future experiments using different levitation gas mediums are necessary to compare the relative volatility of Cu and Zn under more oxidizing and reducing conditions.

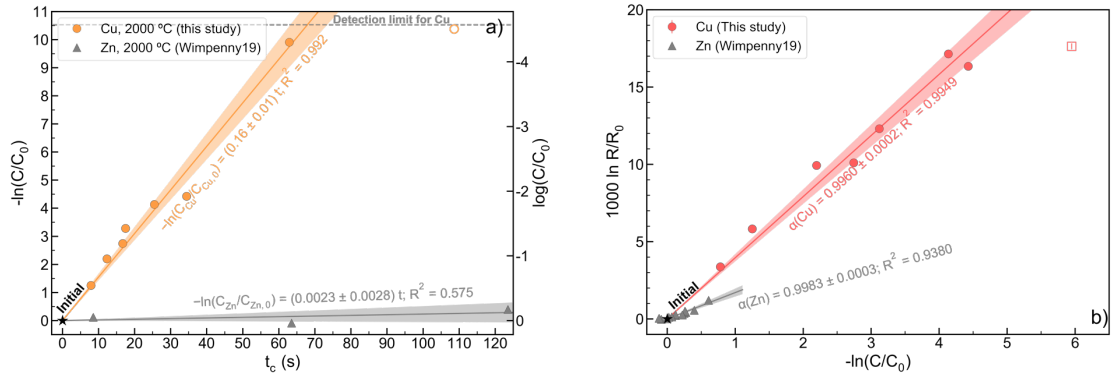

Figure 5. Comparison of Cu and Zn evaporative loss and isotope fractionation in laser levitation experiments. a) Relative change of Cu and Zn concentration ($-\ln C/C_0$) as a function of corrected duration (t_c); b) Copper ($^{65/63}$Cu) and Zn ($^{66/64}$Zn) isotope fractionation as a function of evaporative loss. Straight lines in each figure show linear fitting of the trends for Cu and Zn, respectively. The shaded regions represent 2σ error of the fitting. Experimental data for Zn are from Wimpenny et al. (2019).

Overall, the comparison of Cu and Zn evaporation in laser levitation experiments with a similar setup shows that Cu is significantly more volatile relative to Zn at related conditions, which is consistent with both the higher degree of Cu loss than Zn in natural tektites (Moynier et al., 2010; Rodovská et al., 2017), and thermodynamic calculations that suggest higher volatility for Cu than Zn under tektite formation conditions (Jiang et al., 2019). We interpret the dominating parameters affecting the volatility differences of Cu and Zn to be the activity coefficient (γ_i) and the equilibrium constant (K) of their evaporation reactions. Future studies on the volatilities of Cu and Zn are recommended to conduct experiments with both elements doped in the same initial samples under different redox conditions.

4.1.2 Isotope fractionation of Cu and Zn in laser levitation experiments

In Fig. 5b, our Cu isotope fractionation data are compared to Zn isotope fractionation data using rhyolitic soil as the starting material (Wimpenny et al., 2019). As can be seen in the figure, despite the dramatic differences in their volatilities demonstrated by laser levitation experiments, the isotope fractionation trends for Cu and Zn show similarities. One important observation for both Cu and Zn experiments is the lack of temperature dependence for the isotope fractionation factor. Data points plotted in Fig. 5b include experiments from 1750 to 2150 ºC for Cu, and from 1600 to 2200 ºC for Zn. Nonetheless, the 400 to 600 ºC difference in the experimental temperature did not affect the isotope fractionation factors of Cu and Zn in a measurable way, consistent with a kinetic process driving the isotope fractionation. The trends for Cu and Zn isotope fractionation as a function of their evaporative loss ($-\ln C/C_0$) can both be fit with a linear function, yielding alpha factors of 0.9960 ± 0.0002 for Cu, and 0.9983 ± 0.0003 for Zn (Fig. 5b).

Starting from the Hertz-Knudsen equation (eq. 3), it has been shown in the literature that the isotope fractionation factor of an element during evaporation ($\Delta_{\text{Evaporation}}$) can be calculated as a combined effect of its equilibrium isotope fractionation factor ($\Delta_{\text{Equilibrium}}$) and kinetic isotope fractionation factor (Δ_{Kinetic}) via the following equation (Dauphas et al., 2015; Nie and Dauphas, 2019):

$$\Delta_{\text{Evaporation}} = \Delta_{\text{Equilibrium}} + (1 - s)\Delta_{\text{kinetic}}. \quad (11)$$

In eq. (11), $\Delta_{\text{Evaporation}}$ is related to α in eq. (5) through $\Delta_{\text{Evaporation}} = 1000(\alpha - 1)$, s is the saturation index as defined in eq. (A3) ($s = P_i/P_{i,\text{sat}}, 0 < s < 1$), and Δ_{Kinetic} can be calculated using:

$$\Delta_{\text{Kinetic}} = 1000\left(\frac{\alpha_{ec}^{j}}{\alpha_{ec}^{k}}\sqrt{\frac{M_k}{M_j}} - 1\right), \quad (12)$$

where α_{ec}^{j} and α_{ec}^{k} are the evaporation/condensation constants for two isotopes of an element, and M_j and M_k are the molar masses of the two isotopes.

It is well known since the early work by Urey (1947) and Bigeleisen and Mayer (1947) that equilibrium isotope fractionation decreases rapidly as a function of the square of temperature at relatively high temperatures. Since the laser levitation experiments discussed here were conducted at temperatures over 1600 ºC, the equilibrium isotope fractionation factors ($\Delta_{\text{Equilibrium}}$) for Cu and Zn between the silicate liquid and the vapor phase is expected to be insignificant (e.g. see Xia et al. 2019 as an example for the equilibrium Cu and Zn isotope fractionation between silicate and metal). The kinetic fractionation factors (Δ_{Kinetic}) for Cu or Zn, which represent the isotope fractionation factor for unidirectional evaporation flux and are typically determined by vacuum evaporation experiments, have not been studied in the literature

to the authors' best knowledge. Nonetheless, a reasonable approximation of Δ_{Kinetic} is to use eq. (12) and assume $\alpha_{ec}^{j}/\alpha_{ec}^{k} = 1$ (Nie and Dauphas, 2019).

As a result, the saturation index (s) for Cu and Zn in existing laser levitation experiments can be calculated using eq. (11) to be 0.74 ± 0.01, and 0.89 ± 0.02, respectively. These non-zero s values reflect suppression on both Cu and Zn isotope fractionation by the ambient pressure under which laser levitation experiments were conducted. Compared to free evaporation experiments in vacuum, laser levitation experiments were conducted at one atmosphere in a gas flow, and the pressure was high enough to cause effective re-condensation of evaporated materials back to the sample surface, resulting in a non-zero saturation index and suppressed isotope fractionation factor (Richter et al., 2002; Wimpenny et al., 2019). Similar dependency of isotope fractionation factor on pressure has also been previously reported for K by Yu et al. (2003). The difference in the saturation index (s) for Cu and Zn can be explained by one, or both, of the following two possibilities.

The first possible explanation is that since these two sets of experiments were conducted using two different laser levitation apparatuses, their differences in terms nozzle geometry, gas flow rate, and whether the experiment was conducted in a closed compartment might result in a discrepancy in the effective saturation index. In other words, the aerodynamics might be different in experiments conducted at IPGP for Zn and at IUPUI for Cu, causing a difference in the effective saturation index. Another possibility is that, since the saturation index for Cu and Zn were calculated assuming their kinetic fractionation factors are ideal, the calculated difference between s_{Cu} and s_{Zn} might in fact reflect different degrees of non-ideality in Δ_{Kinetic} for Cu and Zn. When calculating the saturation index (s) using eq. (11), Δ_{Kinetic} was calculated using eq. (12) assuming $\alpha_{ec}^{j}/\alpha_{ec}^{k} = 1$. If this assumption is not true, Δ_{Kinetic} might not be ideal and

could lead to a difference in the saturation index for Cu and Zn. Experimental studies on the kinetic fractionation factors of Cu and Zn in the future will be helpful to verify such a possibility.

According to eq. (11), the isotope fractionation factor for evaporation does not directly depend on melt composition or oxygen fugacity. There still exists a possibility, however, that the melt composition and oxygen fugacity might affect the saturation index (s) or the isotopic difference in the evaporation/condensation constant ($\alpha_{ec}^{j}/\alpha_{ec}^{k}$), therefore introducing an indirect effect on the evaporative isotope fractionation factor ($\Delta_{\text{Evaporation}}$). One important thing to note here is that eq. (11) was derived for a given evaporation reaction. Therefore, the above conclusion on the effect of melt composition and oxygen fugacity assumes that they do not affect the speciation of the element in the silicate melt or the gas phase. In the case of Cu and Zn, this assumption is mostly valid because they almost always reside in natural silicate melts as Cu^{+} and Zn^{2+}, and evaporate in the form of metal (see Sossi et al., 2019). Caution is needed, however, when applying eq. (11) to elements in a composition or oxygen fugacity range that could involve speciation changes.

4.2 Application to Cu isotope data for tektites

Understanding Cu isotope fractionation during tektite formation requires knowledge about the chemical composition of the precursor materials for tektites. This has long been an uncertainty in tektite studies because of the difficulty in precisely identifying the precursor materials for tektites at individual impact strewn fields. A pioneering study by Rodovská et al. (2017), for example, studied sediments from the close surroundings of the Ries impact structure, which are interpreted as precursor materials of moldavites. These sediments vary significantly in mineralogy and Cu concentration (0.82 to 58 ppm), making it difficult to achieve a conclusion on

the composition of the precursor materials for moldavites. A more common approach in the literature, instead, was to assume the average upper continental crust (UCC) as the precursor material for tektites, which has a Cu concentration of 28 ppm (Rudnick and Gao, 2003) and a δ^{65}Cu close to zero (Li et al., 2009; Moynier et al., 2017). Here we follow the latter approach for simplification and assume that the precursor material for tektites contain 28 ppm Cu and has a δ^{65}Cu of 0‰. A discussion on the composition of precursor materials as a source of uncertainty is provided later in the section.

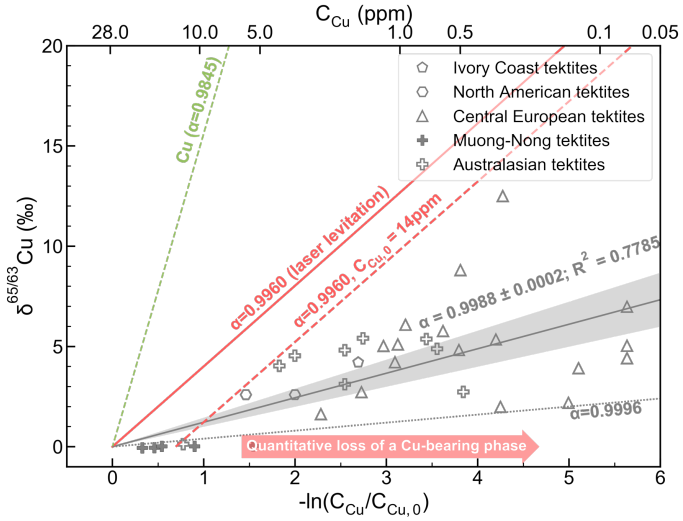

Figure 6. Copper isotope compositions of tektites plotted versus their relative concentration depletion (-ln$C_{Cu}/C_{Cu,0}$). Different types of tektites are distinguished using different symbols (Muong Nong, Australasian, Central European, North American, and Ivory Coast). Note that Muong Nong-type tektites are layered tektites from the Australasian strewn field, and that the group called Australasian tektites contain only splashform types from the Australasian strewn field. Data are from Moynier et al. (2010) and Rodovská et al. (2017). Modeled Rayleigh fractionation trends using α of 0.9960 from our laser levitation experiments, and theoretically calculated α values for Cu during free evaporation are plotted for comparison. The source materials for tektites are assumed to contain 28 ppm Cu and have a δ^{65}Cu of 0‰. The calculated trend using $\alpha = 0.9960$ and an initial Cu concentration of 14 ppm is plotted with the red dashed line. The effect of quantitative loss of a Cu-bearing phase during tektite formation is marked with the red arrow.

Using the assumed chemical composition for the precursor material, Cu isotope fractionation and relative Cu loss (-ln$C_{Cu}/C_{Cu,0}$) for tektites are calculated and plotted in Fig. 6.

564 The tektite data show a general trend correlating Cu isotope fractionation and Cu evaporation
565 loss, which is consistent with a range of α values between 0.9960 and 0.9995 and an average α
566 of 0.9988 ± 0.002 (Fig. 6). The Cu isotope fractionation factor determined by laser levitation
567 experiments is 0.9960, which predicts a fractionation trend higher than the tektite data in Fig. 6
568 (red solid curve). Theoretical α values calculated for free evaporation of Cu ($\alpha = 0.9845$) is also
569 plotted in Fig. 6 for comparison. Overall, it can be seen in Fig. 6 that the observed Cu isotope
570 fractionation in tektites departs significantly from the predicted trend using the theoretical alpha
571 value. The laser levitation experiments, on the other hand, better simulates Cu isotope
572 fractionation in tektites, but the simulation is not perfect.

573 The imperfect simulation of the tektite formation process by laser levitation experiments
574 on Cu isotope fractionation might be attributed to the following factors. First, the estimated
575 average α value for tektite Cu isotope data assumes that all tektite precursor materials initially
576 contained 28 ppm Cu. This is clearly a simplification and in reality, initial Cu concentrations for
577 the tektites are expected to vary from one strewn field to another, and potentially even within a
578 single strewn field. Measurements of chemically diverse sediments from the close surroundings
579 of the Ries impact structure by Rodovská et al. (2017), for example, found Cu concentrations
580 from 0.82 to 58.0 ppm, which would span four natural logarithm units on the horizontal axis if
581 plotted on Fig. 6. Although the impact process is capable of mixing and melting the sediments,
582 therefore reducing the Cu concentration variation in tektite precursor materials, the large range of
583 Cu concentrations in Muong Nong tektites (6 to 18 ppm, Moynier et al., 2010) indicates that this
584 homogenization effect is incomplete. Muong Nong tektites, also called layered tektites, are
585 mainly found in the Australasian strewn field, and are thought to have experienced less extreme
586 heating than splashform tektites, leading to their heterogeneity, higher volatile content, and lesser

587 degree of isotope fractionation (e.g., Koeberl et al., 1984, 1992; Moynier et al., 2010). If the
588 average Cu concentration of the Muong Nong tektites (14 ppm) is used to represent the initial Cu
589 content for tektites, the calculated trend using our experimental α value moves closer to that of
590 natural tektites, but still plots on a steeper gradient to that of the tektite data (dashed red curve in
591 Fig. 6). In the extreme case, if a constant α of 0.9960 is assumed, Cu isotope data of tektites can
592 be explained by the variation in Cu concentration of their precursor materials from 0.4 to 14
593 ppm.

594 The second factor is the host phase for Cu in the precursor materials of tektites.
595 Wimpenny et al. (2019) conducted laser heating experiments on arkose soil, which is composed
596 of alkali feldspar, sodic plagioclase, quartz and limestone fragments, and proposed that a
597 significant proportion of Zn (~70%) might reside in a labile reservoir in the soil. This proportion
598 of Zn was lost rapidly and quantitatively upon heating without causing any isotope fractionation,
599 even for the experiment at 1600 ºC for only 1 s. If a similar reservoir for Cu existed in the
600 precursor materials for tektites, complete loss of this phase might cause Cu depletion without
601 fractionating Cu isotopes, which helps reconcile the difference between the laser levitation
602 experiments and tektite data (Fig.5). Therefore, further studies are needed to verify the existence
603 of such a labile phase, as well as its Cu isotope composition relative to the bulk precursor
604 materials.

605 Lastly, the basaltic composition for the starting material used in our experiments is
606 different from that of the precursor materials for tektites, which are more silicic in composition.
607 The gas composition used in our experiments is Ar, which is also different from the environment
608 for tektite formation (air), especially in terms of oxygen fugacity. As shown in Section 4.1.2 and
609 will be discussed in Section 4.4, melt composition and oxygen fugacity are not expected to have

610 a direct impact on the isotope fractionation factor (α). On the other hand, the aerodynamics of
611 the laser levitation experiments might be different from the tektite formation process, resulting in
612 a difference in the effective degree of saturation (s) in the vapor phase, which in turn could
613 contribute to the observed difference in α (see Section 4.1.2).
614
615 **4.3 Comparison of laser levitation experiments with tektite formation and Moon formation**
616 **conditions**
617 Combining eq. (11) with the Rayleigh fractionation equation (eq. 5 and 6), the isotope
618 fractionation of an element ($\delta - \delta_0$) can be related to its degree of depletion ($\ln F$) and saturation
619 index (s) through the following equation (Nie and Dauphas, 2019):
620 $$\delta - \delta_0 \approx \left[\Delta_{\text{Equilibrium}} + (1-s)\Delta_{\text{kinetic}}\right]\ln F \approx (1-s)\Delta_{\text{kinetic}}\ln F. \quad (13)$$
621 For an evaporation process with a given degree of saturation (s) for the moderately volatile
622 elements, plotting their isotope fractionation ($\delta - \delta_0$) versus $\Delta_{\text{kinetic}}\ln F$ should show a straight
623 line with a slope of $(1-s)$. Most previous studies on kinetic isotope fractionation of moderately
624 volatile elements in tektites and lunar samples focused on understanding individual elements, or
625 combining two to three isotope systems. Equation (13), however, provides a way to
626 simultaneously compare all the isotope systems available in the literature to understand the
627 geological/planetary processes that formed tektites and the Moon.

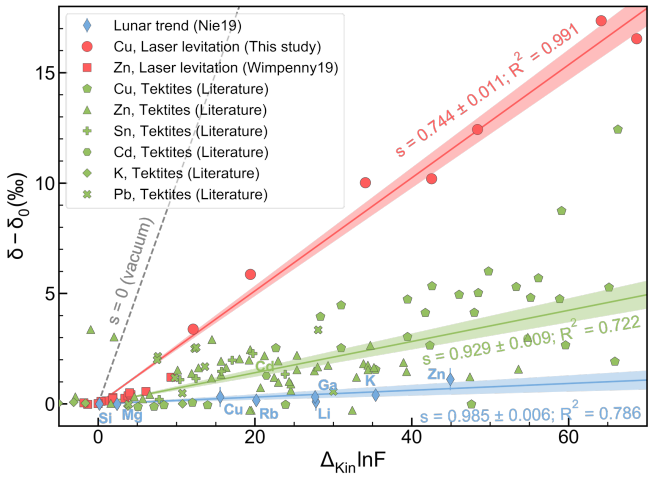

Figure 7. Assessment of the saturation index ($s = P_i/P_{i,\mathrm{sat}}$) experienced by moderately volatile elements. Isotope fractionation of an element during evaporation ($\delta - \delta_0$) is plotted versus the product of the kinetic fractionation factor ($\Delta_{\mathrm{Kinetic}}$) and the natural logarithm of its concentration depletion relative to the precursor material ($\ln F$). Kinetic fractionation factors ($\Delta_{\mathrm{Kinetic}}$) are assumed to be ideal. The lunar trend is modified from Nie and Dauphas (2019), updated with more recent abundance estimation by Ni et al. (2019). Tektite data are from Wombacher et al. (2003); Moynier et al. (2009); Moynier et al. (2010); Rodovská et al. (2017); Jiang et al. (2019); Wimpenny et al. (2019); Creech et al. (2019); and Ackerman et al. (2020). Laser levitation data for Zn are from Wimpenny et al. (2019). The lunar trend and the laser levitation experiment trend are fit with a linear function, which are shown in solid lines in the figure, with the shadowed regions representing 2 standard errors of the fitting. Note that the slope of the linear fitting is 1-*s*, while the fitting results in the figure are for *s*. The expected trend for free-evaporation in vacuum (*s*=0) is also shown for comparison.

It has been shown by Nie and Dauphas (2019) that the isotope fractionation of Li, Si, Mg, Ga, Cu, Zn, Rb, and K for the bulk silicate Moon falls on a linear trend consistent with a saturation index of *s*=0.989, indicating a lunar volatile depletion process under a partially saturated (99%) condition. The fact that different elements evaporated under similar degrees of saturation indicates a dynamic balance between the net evaporation flux and the vapor removal in the protolunar disk (Nie and Dauphas, 2019). Note that applying eq. (13) to isotope fractionation of the bulk silicate Moon does not take into account other processes during Moon formation (e.g. core formation), which could sometimes be oversimplistic. In Fig. 7, the lunar isotope fractionation trend from Nie and Dauphas (2019) is plotted after recalculating $\ln F$ using

652 the more recent estimation of Li, Ga, Cu, Zn, Rb, and K concentrations in the primitive lunar
653 mantle by Ni et al. (2019). As shown in Fig. 7, the replotted trend for lunar moderately volatile
654 elements is very similar to that in Nie and Dauphas (2019) and is consistent with an *s* value of
655 0.985.

656 Using the same approach, tektite isotope data for $^{41}K/^{39}K$ (Jiang et al., 2019), $^{114}Cd/^{112}Cd$
657 (Wombacher et al., 2003), $^{122}Sn/^{118}Sn$ (Creech et al., 2019), $^{66}Zn/^{64}Zn$ (Moynier et al., 2009;
658 Wimpenny et al., 2019), $^{65}Cu/^{63}Cu$ (Moynier et al., 2010; Rodovská et al., 2017), and $^{208}Pb^{204}/Pb$
659 (Ackerman et al., 2020) are compared by plotting their isotope fractionation ($\delta - \delta_0$) versus
660 $\Delta_{\text{kinetic}} \ln F$ in Fig. 7. Earlier tektite data for $^{41}K/^{39}K$ measured by secondary ion mass
661 spectrometry (Humayun and Koeberl, 2004; Herzog et al., 2008) are consistent with those
662 reported in Jiang et al. (2019), but they are excluded in the plot here because of the higher
663 analytical uncertainties. Note that tektites have also been studied for $^{7}Li/^{6}Li$ (Magna et al., 2011;
664 Rodovská et al., 2016), $^{11}B/^{10}B$ (Chaussidon and Koeberl, 1995), and $^{26}Mg/^{24}Mg$ (Esat and
665 Taylor, 1986; 1987), but the isotope fractionation was found to be small. Therefore, these
666 elements are excluded from the plot for simplification. If plotted in Fig. 7, these three elements
667 would be near the origin, similar to K for tektites. The Δ_{kinetic} values used for the plot for
668 different elements are calculated using eq. (12) assuming ideality ($\alpha_{ec}^{j}/\alpha_{ec}^{k} = 1$). Chemical
669 composition of the precursor material for tektites is adopted from the same references for the
670 isotope data, which typically used the upper continental crust or the Muong Nong-type tektites as
671 an approximation. This precursor material is assumed to contain 2.32 wt% K, 125 ppb Cd, 1.6
672 ppm Sn, 100 ppm Zn, 20 ppm Pb, and 28 ppm Cu, and has an isotope composition of $\delta^{41}K$ = -
673 0.48‰, $\delta^{114}Cd$ = 0.24‰, $\delta^{122}Sn$ = 0.25‰, $\delta^{66}Zn$ = 0.28‰, $^{208}Pb/^{204}Pb$ = 39.15275, and $\delta^{65}Cu$ =
674 0.07‰. This assumption of a single composition for the precursor material is for simplification.

675 But we would like to emphasize that adjusting the composition of the precursor material in a
676 reasonable range does not affect the general trend for the tektite data in Fig. 7.

677 As shown in Fig. 7, the tektite isotope data span a much wider range compared to the
678 lunar trend. This is understandable because the lunar trend is based on the estimated average
679 composition for the bulk silicate Moon, while the tektite data are collected on individual tektite
680 samples from multiple independent strewn fields worldwide. The scatter in tektite data might
681 reflect: a) heterogeneity in the precursor materials; b) existence of quantitative evaporation that
682 compromised the isotope fractionation, as discussed in Section 4.2; and/or c) variations in the
683 physical conditions for tektite formation. Despite the scatter in tektite data, different elements are
684 roughly consistent, broadly defining a tektite trend with an average saturation index of 0.929
685 (Fig. 7). The tektite trend lies above the lunar trend in Fig. 7, indicating that the tektite formation
686 process is evidently more undersaturated (averaged 93%, as low as ~87%) compared to Moon
687 formation (~99%).

688 The laser levitation experiments, on the other hand, fall on the high end of the tektite data
689 and are consistent with a low saturation index (s) of 0.74 ± 0.01. The lower degree of saturation
690 for laser levitation experiments relative to tektites indicates that, although laser heating of an
691 aerodynamically levitated melt sphere is a good experimental simulation of the tektite formation
692 process, these two kinetic processes are not identical in terms of the effective degree of vapor
693 saturation. Further studies on molecular dynamic calculations and aerodynamic simulations will
694 be necessary to quantitatively explain such a difference. Future levitation experiments varying
695 gas flow, nozzle geometry, and ambient pressure may also contribute to our understanding of the
696 effect of saturation index on chemical and isotopic fractionation attending partial vaporization.

Although the silicate Moon likely experienced a kinetic process (e.g. evaporation in the protolunar disk) dramatically different from the laser levitation experiments and the tektite formation process, the observed difference in the saturation index (Fig. 7) can potentially be attributed to the vapor pressure. Laser levitation experiments were conducted at 1 bar ambient pressure. Tektites formed in an impact vapor plume, which likely had a pressure higher than 1 bar. Theoretical simulation in Stöffler et al. (2002), for example, showed that tektite-like particles experienced dynamic pressures as high as 0.4 bar, in addition to the ambient pressure. On the other hand, Wang and Jacobsen (2016) argued that the suppressed K isotope fractionation of the Moon was consistent with a pressure of >10 bar. Although further studies are needed, the increasing vapor saturation index from laser levitation experiments to tektites and bulk silicate Moon might be indicative of the vapor pressure related to their formation.

4.4 Further ramifications on evaporative isotope fractionation for moderately volatile elements

4.4.1 Starting material composition

Compared to the arkose soil and rhyolite soil used in Wimpenny et al. (2019), a synthetic basalt glass was used in this study as the starting material. Although a soil sample might better represent the precursor materials of tektites, the uncertainties on the hosting phase for Cu might complicate the interpretation of the experiment results. The arkose soil in Wimpenny et al. (2019), for example, seems to contain a highly volatile Zn-bearing phase that completely evaporates immediately upon heating, making it more difficult to constrain the initial Zn content for calculating the Zn isotope fractionation factor. Therefore, in this study a homogenous synthetic basalt glass is used as the starting material to avoid possible complications caused by

heterogeneous distribution of Cu in soil samples. In addition to being homogeneous in composition, using a synthetic glass also allows a higher initial Cu concentration (1129 ppm) compared to the precursor materials of tektites (28 ppm), which significantly extends the possible experiment duration before the Cu concentration drops below the detection limit. Here a basaltic composition is selected for the synthetic glass because it has higher Cu solubility (Zajacz et al., 2013) and lower viscosity (Hui and Zhang, 2007) compared to a rhyolitic composition, making it easier to synthesize a bubble-free homogeneous glass with high Cu concentration.

The effect of melt composition on the volatility of Cu is reflected in its activity coefficient (γ_i) and the equilibrium constant (K) of its evaporation reaction (eq. 9). Experiments by Zajacz et al. (2013), however, demonstrated that Cu solubility is similar for rhyolite and basalt in a S-free system, and higher in basalt than in rhyolite in a S-bearing system at < 1000 ºC. If this observation can be extrapolated to our experimental temperatures, using a rhyolitic composition for the starting material will cause Cu to be even more volatile than observed. Therefore, the observed higher volatility of Cu in our experiments than that of Zn in the experimental study of Wimpenny et al. (2019) is not due to the composition effect. Furthermore, despite potential indirect effects, melt composition is not expected to have a direct impact on the evaporative isotope fractionation factor according to eq. (11) (see Section 4.1.2).

4.4.2 "Bubble-stripping" model

Jiang et al. (2019) conducted *in situ* measurements on Zn, Cu, and K concentrations, as well as Zn and K isotope ratios along a cross section of a Hainan splashform tektite, and found one point along the traverse that is high in Zn concentration and light in Zn isotope ratios. The authors hypothesized that the anomalous data point was likely the result of a "trapped" vapor

743 bubble mixed with the residual melt – a side effect from the "bubble-stripping" process.
744 Originally proposed by Melosh and Artemieva (2004), "bubble-stripping" refers to the process
745 by which low density vapor bubbles form in the melt as other volatiles exsolve; the bubbles
746 rapidly move to the surface and burst, releasing their vapor load.

747 Such a process, if it occurred during tektite formation or laser levitation experiments,
748 would introduce evaporation into a closed vapor phase, potentially under pressures higher than 1
749 bar (Melosh and Artemieva 2004). Moderately volatile elements evaporated via this mechanism
750 likely experienced a higher effective degree of vapor saturation (s) compared to evaporation
751 from the outer surface of tektites or laser levitation experiment samples, causing suppression of
752 the isotope fractionation factor. Therefore, the effect of the "bubble-stripping" mechanism is
753 equivalent to an increase in the effective degree of vapor saturation (s), which suppresses the
754 evaporative isotope fractionation factor.

755 Copper loss in our laser levitation experiments is likely due to direct evaporation at the
756 melt surface rather than being removed through "bubble-tripping". This is because, the starting
757 material used in this study is an anhydrous basalt containing less than ~10 ppm H_2O, therefore
758 lacks the key ingredient for the bubble formation (Melosh and Artemieva 2004). One the other
759 hand, the precursor materials for natural tektites could be water-rich, and the "bubble-stripping"
760 mechanism might help explain their suppressed Cu isotope fractionation.

761

762 *4.4.3 The role of diffusion*

763 Previous studies by Moynier et al. (2010) and Creech et al. (2019) proposed the existence
764 of a diffusion-limited regime within the tektite to explain the higher magnitude of isotope
765 fractionation in Cu relative to Sn and Zn despite its lower volatility. Although the diffusion-

766 limited regime is consistent with the significantly higher diffusivity of Cu than Zn and Sn in
767 silicate melts (Baker and Watson, 1988; Yang et al., 2016; Ni et al., 2017; Ni et al., 2018), it is
768 unlikely the dominating mechanism for evaporative isotope fractionation in laser levitation
769 experiments or tektites. The reasons are as follows.

770 First, based on our laser levitation experiments and thermodynamic modeling of Jiang et
771 al. (2019), Cu appears to be more volatile than Zn under tektite formation conditions, making it
772 unnecessary to explain the higher degrees of Cu loss and Cu isotope fractionation compared to
773 Zn in tektites using a separate mechanism.

774 Second, our laser levitation experiments show clear evidence that Cu concentration
775 decreases exponentially as a function of time, consistent with an evaporation-dominated process.
776 If Cu loss is dominated by Cu diffusion in the melt, however, Cu concentration is expected to
777 decay as a function of $\sqrt{t}$ (Zhang, 2008), which is not consistent with the observation.

778 Third, *in situ* measurements for concentration profiles of Cu, Zn, and K in a Hainan
779 tektite reported by Jiang et al. (2019) found no clear evidence to support diffusion limitation
780 even across several centimeters, making it unlikely for diffusion control to occur in our
781 experiments, where samples are only ~2 mm in diameter and the thermal history is similar to that
782 of natural tektites.

783 Moreover, compared to convective transport, diffusion transport is a kinetic process that
784 can cause additional isotope fractionation because the lighter isotopes of an element transports
785 faster than heavier isotopes in silicate melts (e.g. Richter et al., 2009):

786 $$\frac{D_i}{D_j} = \left(\frac{M_j}{M_i}\right)^{\beta}, \quad (14)$$

787 where D_i and D_j are the diffusivities of two isotopes of an element, M_i and M_j are their
788 respective molar masses, and β is a coefficient that is usually determined experimentally ($\beta <$

0.5). In laser levitation experiments or tektite formation processes, moderately volatile elements are transported to the melt-vapor interface by convection and/or diffusion, and then lost to the vapor phase by evaporation. Assuming a diffusion-limited regime, the relative importance of diffusive transport depends on the diffusivity of an element. Since Cu^{+} has higher diffusivity than Zn and Sn in silicate melts (Baker and Watson, 1988; Yang et al., 2016; Ni et al., 2017), the higher percentage of diffusive transport is expected to cause additional isotope fractionation in Cu, leading to lower effective alpha values compared to Zn and Sn. As can be seen in Fig. 7, Cu isotope data in tektites appear to be on the same trend as Zn and Sn, and the higher isotope fractionation in Cu is consistent with its higher degrees of evaporative loss.

Overall, although the role of diffusion in tektite formation cannot be fully excluded, it is unlikely to be the dominating factor for the isotope fractionation of moderately volatile elements in tektites based on current data. Future experiments should confirm these ideas by measuring compositions in a cross-section of an experimental sample to check carefully for any gradients from the center to the edge.

5. Conclusions

In this paper, we report the first experimental study on Cu isotope fractionation during evaporation to simulate tektite formation. Our experiments clearly demonstrate a progressive enrichment in the heavier isotope of Cu correlated with its evaporative loss as a function of experiment duration, which is consistent with the elevated $^{65}Cu/^{63}Cu$ ratios previously reported in tektites. In our experiments, rapid loss of Cu by over four orders of magnitude occurred within 60 seconds, causing fractionation of $\delta^{65}Cu$ by up to ~18‰ in the residue melt. A well-defined fractionation factor (α) of 0.9960 ± 0.0002 can be calculated from our experiments.

Comparing with previous experiments on Zn evaporation using a similar experimental setup, we found that Cu evaporation loss is significantly faster than Zn in laser levitation experiments at 2000 ºC. Copper concentration decreased by over four orders of magnitude within 60 s, while Zn only depleted by ~33% in 120 s. The large differences in the evaporation rates of Cu and Zn can be attributed to their differences in activity coefficient (γ) and the equilibrium constant for the evaporation reaction (K). The fractionation factor (α) yielded for Cu (0.9960 ± 0.0002) differs slightly from that of Zn (0.9983 ± 0.0003). Such a difference can be explained by either the higher degree of non-ideality in kinetic isotope fractionation factor ($\Delta_{kinetic}$) for Zn, or slight differences in the experimental setup between IUPUI and IPGP that led to different effective saturation indexes (s) for the experiments.

We also demonstrate a way to simultaneously compare isotope fractionation of multiple isotope systems in the bulk silicate Moon, tektites, and laser levitation experiments by correcting the degree of depletion using their respective kinetic isotope fractionation factor. We show that isotope fractionation trends in the bulk silicate Moon, tektites, and laser levitation experiments are consistent with their formation under various degrees of vapor saturation (~99%, ~93%, and ~74%) that is well above the case for free-evaporation (0%). The tektite isotope fractionation trend appears to be more scattered compared to the lunar trend, largely due to uncertainty in the compositions of tektite precursor materials. Laser-heated aerodynamic levitation experiments show Cu and Zn isotope fractionation that is consistent with slightly lower degrees of vapor saturation compared to tektites. The progressively higher vapor saturation index estimated for laser levitation experiments, tektites, and bulk silicate Moon may be attributed to the differences in vapor pressure during their formation.

Acknowledgment

The authors thank M. F. Horan for assistance with column chemistry and T. D. Mock for help with the MC-ICPMS. This manuscript benefited from constructive reviews by M. Humayun, F. Wombacher, P. Savage, and an anonymous reviewer. P. Ni acknowledges N. Nie for helpful discussions that contributed to this work. P. Ni was supported by a Carnegie Postdoctoral Fellowship while working on this project. This research is partly supported by NSF grant EAR1851736 to AS and CAM.

843 **Table 1.** Experimental conditions, Cu concentrations, and isotopic compositions for all experimentally heated basalt glass samples.

Sample	d_0 (mm)	d (mm)	M_0 (mg)	M (mg)	ΔM (%)	t_r (s)	t_c (s)	T (ºC)	C_{Cu}	δ^{65}Cu (‰)	2 s.e.	n
Et1Cu	-	-	-	-	-	-	-	-	1185	3.46	0.02	12
Cu 1.15	2.3	2.42	19.664	-	-	-	-	-	1129	3.71	0.03	4
Cu 1.12	2.42	2.36	20.044	19.822	1.11	8	17.9	1750	517	7.10	0.04	8
Cu 1.14	2.38	2.32	19.072	18.486	3.07	4	6.7	2150	50	16.14	0.06	8
Cu 1.17	2.34	2.31	20.008	19.270	3.69	8	10.0	2150	34	*n.d.*	-	-
Cu 1.18	2.31	2.39	19.958	18.632	6.64	16	18.6	2150	35	*n.d.*	-	-
Cu 1.2	2.43	2.36	20.040	19.180	4.29	30	33.8	2150	2.7	21.57	0.19	6
Cu 1.3	2.43	2.19	20.196	18.632	7.74	60	59.1	2150	*0.028*	*b.d.*	-	-
Cu 1.4	2.44	2.33	20.160	17.724	12.08	90	75.4	2150	*0.028*	*b.d.*	-	-
Cu 1.5	2.44	2.33	20.154	17.986	10.76	120	84.5	2150	0.31	*b.d.*	-	-
Cu 1.13	2.41	2.41	19.558	19.306	1.29	4	7.9	2000	323	9.59	0.11	8
Cu 1.11	2.43	2.41	20.008	19.590	2.09	8	12.3	2000	126	13.66	0.06	8
Cu 1.9	2.44	2.30	20.220	19.720	2.47	16	16.7	2000	73	13.91	0.05	8
Cu 1.19	2.31	2.39	19.964	19.296	3.35	16	17.5	2000	42	*n.d.*	-	-
Cu 1.10	2.42	2.42	20.140	19.388	3.73	16	25.5	2000	18	21.07	0.03	6
Cu 1.7	2.41	2.30	20.082	19.572	2.54	30	34.4	2000	12	20.25	0.06	6
Cu 1.8	2.42	2.33	20.046	18.822	6.11	60	62.9	2000	*0.056*	*b.d.*	-	-
Cu 1.1	2.41	2.42	19.902	17.900	10.06	120	108.6	2000	*0.035*	*b.d.*	-	-

844 Note: d_0 and d are diameters for the glass sphere before and after the heating experiment; M_0 and M are the masses of the glass spheres
845 before and after the experiment; t_r is the recorded duration at the peak temperature; t_c is corrected experiment duration using Eq. (1)
846 for the evaporation process; and T is the experiment temperature. In the table, "*n.d.*" means "not determined", "*b.d.*" means "below
847 detection limit", and Cu concentrations close to the detection limit are italicized.
848
849

*E-mail: pni@carnegiescience.edu

APPENDIX A: SOLUTION OF THE HERTZ-KNUDSEN EQUATION FOR EVAPORATION OF AN ELEMENT FROM A MELT SPHERE

The derivation below is very similar to that in Sossi et al. (2019), but with some minor changes. For a metal oxide component of the melt that evaporates to a gaseous species with a different valence state, the chemical reaction is:

$$\mathrm{MO}_{(x+n)/2}(l) = \mathrm{MO}_{x/2}\,(g) + \frac{n}{4}\mathrm{O}_2, \tag{A1}$$

in which M is the metal, x is its charge in the gaseous phase, and n is the number of electrons transferred in the reaction. According to the Hertz-Knudsen equation, the net evaporation flux of M from the melt sphere is (e.g. Richter et al., 2007; Dauphas et al., 2015; Sossi et al., 2019):

$$\frac{dn_i}{dt} = -4\pi r^2 \frac{\alpha_{ec}(P_{i,\mathrm{sat}} - P_i)}{\sqrt{2\pi R M_i T}}, \tag{A2}$$

in which dn_i/dt is the net evaporation flux in mol/s; r is the radius of the melt sphere in m; $P_{i,\mathrm{sat}}$ is the equilibrium partial pressure of element i in Pa; P_i is the partial pressure of element i at the surface in Pa; M_i is its molar mass in kg/mol; R is the gas constant (R=8.314 J/mol/K); T is the temperature in K; and α_{ec} is the dimensionless evaporation/condensation coefficient (fraction of molecules sticking onto the surface, $0 < \alpha_{ec} < 1$). Define the saturation index s as:

$$s = P_i/P_{i,\mathrm{sat}}, \tag{A3}$$

and convert n_i to its mole percent (X_i) in the melt sphere with n_{tot} total molecules using:

$$X_i = \frac{n_i}{n_{\mathrm{tot}}} = \frac{n_i}{4\pi r^3 \rho/(3M_{\mathrm{melt}})}, \tag{A4}$$

eq. (A2) can be converted to:

$$\frac{dX_i}{dt} = -\frac{3\alpha_{ec}(1-s)P_{i,\mathrm{sat}}}{r\rho}\frac{M_{\mathrm{melt}}}{\sqrt{M_i}}\sqrt{\frac{1}{2\pi RT}}. \tag{A5}$$

Here M_{melt} is the molar mass of the melt in g/mol, and ρ is the density of the melt in kg/m^3.

*E-mail: pni@carnegiescience.edu

Since the saturation pressure of element *i* can be calculated using the equilibrium constant (K) of reaction (A1) through:

$$P_{i,\mathrm{sat}} = \frac{KX_i\gamma_i}{f(O_2)^{\frac{n}{4}}}, \tag{A6}$$

where γ_i is the activation coefficient of element *i* in the melt and $f(O_2)$ is the oxygen fugacity, eq. (A5) can be further converted to:

$$\frac{dX_i}{X_i} = -\frac{3\alpha_{ec}(1-s)\gamma_i K}{r\rho f(O_2)^{\frac{n}{4}}}\frac{M_{\mathrm{melt}}}{\sqrt{M_i}}\sqrt{\frac{1}{2\pi RT}}dt. \tag{A7}$$

Integrating Eq. A7 on both sides with respect to dX_i and dt yields:

$$ln\frac{X_i}{X_{i,0}} = -\frac{3\alpha_{ec}(1-s)\gamma_i K}{r\rho f(O_2)^{\frac{n}{4}}}\frac{M_{\mathrm{melt}}}{\sqrt{M_i}}\sqrt{\frac{1}{2\pi RT}}t, \tag{A8}$$

where $X_i/X_{i,0}$ denotes the mole fraction of an element *i* at a given time relative to its initial mole percent in the melt.

The mole fraction of an element (X_i) in the melt is related to its concentration (C_i, in wt%) through:

$$C_i = \frac{X_i M_i}{M_{melt}} \times 100\ wt\%. \tag{A9}$$

If the molar mass change of the melt phase during evaporation is ignored, eq. (A8) can also be expressed in the form of elemental concentration as:

$$ln\frac{C_i}{C_{i,0}} = -\frac{3\alpha_{ec}(1-s)\gamma_i K}{r\rho f(O_2)^{\frac{n}{4}}}\frac{M_{\mathrm{melt}}}{\sqrt{M_i}}\sqrt{\frac{1}{2\pi RT}}t, \tag{A10}$$

APPENDIX B: DURATION CORRECTION FOR EVAPORATION EXPERIMENTS WITH A TIME-DEPENDENT THERMO HISTORY

As derived above in Appendix A, evaporation loss of an element *i* with the chemical reaction A1 can be described using Eq. (A7). Among all the parameters on the right-hand side of Eq. (A7), assume only the equilibrium constant *K* is temperature-dependent, it can be calculated using thermodynamic parameters through:

$$K = \exp\left(\frac{\Delta G}{-RT}\right) = \exp\left(\frac{\Delta H - T\Delta S}{-RT}\right) = \exp\left(-\frac{\Delta H}{RT}\right) \cdot \exp\left(\Delta S/R\right), \quad \text{(B1)}$$

where ΔH and ΔS are the enthalpy and entropy for reaction A1, respectively. Define a temperature-independent parameter a as:

$$a = \frac{3\alpha_{ec}\gamma_i \exp\left(\frac{\Delta S}{R}\right)}{r\rho f(O_2)^{\frac{1}{4}}} \cdot (1-s) \cdot \frac{M_{\text{melt}}}{\sqrt{M_i}} \cdot \sqrt{\frac{1}{2\pi R}}, \quad \text{(B2)}$$

and substitute into eq. (A7), a simplified form of eq. (A7) is obtained as:

$$\frac{dX_i}{X_i} = -a \exp\left(-\frac{\Delta H}{RT}\right)/\sqrt{T} \cdot dt. \quad \text{(B3)}$$

For an ideal experiment without heating, quenching, or any temperature fluctuation, the relative change of concentration for element *i* ($X_i/X_{i,0}$) in the evaporating melt sphere at the target temperature T_0 for a duration of t_c can be obtained by integrating both sides of eq. (B3) that yields:

$$ln\frac{X_i}{X_{i,0}} = -a \exp\left(-\frac{\Delta H}{RT_0}\right)/\sqrt{T_0} \cdot t_c. \quad \text{(B4)}$$

In reality, an experiment has a thermal history involving heating up from ambient temperature to the target temperature, quenching from the target temperature to ambient temperature, and temperature fluctuations during the experiment. Therefore, integration of the right-hand side of eq. (B3) can be done numerically using the thermal history as follows:

$$ln\frac{X_i}{X_{i,0}} = -\int a\exp\left(-\frac{\Delta H}{RT}\right)/\sqrt{T}\cdot dt = \sum_{i=0}^{N}\left[-a\exp\left(-\frac{\Delta H}{RT_{i,i+1}}\right)/\sqrt{T_{i,i+1}}(t_{i+1}-t_i)\right], \quad \text{(B5)}$$

where N is the number of data points recorded in the thermal history; t_i is the time recorded at the ith data point; $T_{i,i+1}$ is the average temperature recorded at t_i and t_{i+1}. Combining eq. (B4) and eq. (B5) we get the corrected duration as:

$$t_c = \frac{\int \exp\left(\frac{\Delta H}{-RT}\right)/\sqrt{T}\cdot dt}{\exp\left(\frac{\Delta H}{-RT_0}\right)/\sqrt{T_0}} = \frac{\sum_{i=0}^{N}\left[\exp\left(-\frac{\Delta H}{RT_{i,i+1}}\right)/\sqrt{T_{i,i+1}}(t_{i+1}-t_i)\right]}{\exp\left(\frac{\Delta H}{-RT_0}\right)/\sqrt{T_0}}. \quad \text{(B6)}$$

In this study, a ΔH of 264 kJ/mol/K from Sossi et al. (2019) for Cu evaporation is used for the duration correction. In the above calculations, certain parameters such as the saturation index (s) and the evaporation/condensation parameter (α_{ec}) are assumed to be temperature-independent, which might not be true for the evaporation experiments. Nonetheless, when correcting for heating-up and quenching, the most sensitive parameter is the equilibrium constant K, which decays exponentially as temperature decreases. With a ΔH of 264 kJ/mol/K, it effectively reduces the evaporation flux by one order of magnitude when temperature decreases from 2000 ºC to 1600 ºC. For the other term in eq. (B4), for example, $\sqrt{T}$ only reduces by <10% during the same temperature change. Therefore, potentially small variations in parameters assumed to be temperature independent are less important for the duration correction.

925 # References

926 Ackerman L., Žák K., Skála R., Rejšek J., Křížová Š., Wimpenny J. and Magna T. (2020) Sr-Nd-Pb isotope
927 systematics of Australasian tektites: Implications for the nature and composition of target materials and possible
928 volatile loss of Pb. *Geochim. Cosmochim. Acta* **276**, 135–150.
929 Alderman O. L. G., Lazareva L., Wilding M. C., Benmore C. J., Heald S. M., Johnson C. E., Johnson J. A., Hah H.-
930 Y., Sendelbach S., Tamalonis A., Skinner L. B., Parise J. B. and Weber J. K. R. (2017a) Local structural
931 variation with oxygen fugacity in Fe2SiO4+x fayalitic iron silicate melts. *Geochim. Cosmochim. Acta* **203**, 15–
932 36.
933 Alderman O. L. G., Wilding M. C., Tamalonis A., Sendelbach S., Heald S. M., Benmore C. J., Johnson C. E.,
934 Johnson J. A., Hah H.-Y. and Weber J. K. R. (2017b) Iron K-edge X-ray absorption near-edge structure
935 spectroscopy of aerodynamically levitated silicate melts and glasses. *Chem. Geol.* **453**, 169–185.
936 Artemieva N., Karp T. and Milkereit B. (2004) Investigating the Lake Bosumtwi impact structure: Insight from
937 numerical modeling. *Geochem. Geophys. Geosystems* **5**. Available at:
938 https://agupubs.onlinelibrary.wiley.com/doi/abs/10.1029/2004GC000733 [Accessed October 4, 2019].
939 Baker D. R. and Watson E. B. (1988) Diffusion of major and trace elements in compositionally complex Cl- and F-
940 bearing silicate melts. *J. Non-Cryst. Solids* **102**, 62–70.
941 Barnes V. E. (1958) Properties of tektites pertinent to their origin. *Geochim. Cosmochim. Acta* **14**, 267–278.
942 Bigeleisen J. and Mayer M. G. (1947) Calculation of Equilibrium Constants for Isotopic Exchange Reactions. *J.*
943 *Chem. Phys.* **15**, 261–267.
944 Chaussidon M. and Koeberl C. (1995) Boron content and isotopic composition of tektites and impact glasses:
945 Constraints on source regions. *Geochim. Cosmochim. Acta* **59**, 613–624.
946 Chen H., Moynier F., Humayun M., Bishop M. C. and Williams J. T. (2016) Cosmogenic effects on Cu isotopes in
947 IVB iron meteorites. *Geochim. Cosmochim. Acta* **182**, 145–154.
948 Creech J. B., Moynier F. and Koeberl C. (2019) Volatile loss under a diffusion-limited regime in tektites: Evidence
949 from tin stable isotopes. *Chem. Geol.* **528**, 119279.
950 Dauphas N., Poitrasson F., Burkhardt C., Kobayashi H. and Kurosawa K. (2015) Planetary and meteoritic Mg/Si and
951 δ30Si variations inherited from solar nebula chemistry. *Earth Planet. Sci. Lett.* **427**, 236–248.
952 Esat T. M. and Taylor S. R. (1986) MG Isotope Composition of Ivory Coast Microtektites. *Lunar Planet. Sci. Conf.*
953 **17**, 210–211.
954 Esat T. M. and Taylor S. R. (1987) MG Isotopic Composition of Microtektites and Flanged Australite Buttons.
955 *Lunar Planet. Sci. Conf.* **18**. Available at: http://adsabs.harvard.edu/abs/1987LPI....18..267E [Accessed
956 December 17, 2019].
957 Glass B. P. (1990) Tektites and microtektites: key facts and inferences. *Tectonophysics* **171**, 393–404.
958 Guo C. and Zhang Y. (2018) Multicomponent diffusion in basaltic melts at 1350 °C. *Geochim. Cosmochim. Acta*
959 **228**, 190–204.
960 Herzog G. F., Alexander C. M. O., Berger E. L., Delaney J. S. and Glass B. P. (2008) Potassium isotope abundances
961 in Australasian tektites and microtektites. *Meteorit. Planet. Sci.* **43**, 1641–1657.
962 Herzog G. F., Moynier F., Albarède F. and Berezhnoy A. A. (2009) Isotopic and elemental abundances of copper
963 and zinc in lunar samples, Zagami, Pele's hairs, and a terrestrial basalt. *Geochim. Cosmochim. Acta* **73**, 5884–
964 5904.
965 Holzheid A. and Lodders K. (2001) Solubility of copper in silicate melts as function of oxygen and sulfur fugacities,
966 temperature, and silicate composition. *Geochim. Cosmochim. Acta* **65**, 1933–1951.
967 Howard K. T. (2011) Volatile enhanced dispersal of high velocity impact melts and the origin of tektites. *Proc.*
968 *Geol. Assoc.* **122**, 363–382.
969 Hui H. and Zhang Y. (2007) Toward a general viscosity equation for natural anhydrous and hydrous silicate melts.
970 *Geochim. Cosmochim. Acta* **71**, 403–416.
971 Humayun M. and Koeberl C. (2004) Potassium isotopic composition of Australasian tektites. *Meteorit. Planet. Sci.*
972 **39**, 1509–1516.
973 Jiang Y., Chen H., Fegley B., Lodders K., Hsu W., Jacobsen S. B. and Wang K. (2019) Implications of K, Cu and
974 Zn isotopes for the formation of tektites. *Geochim. Cosmochim. Acta* **259**, 170–187.
975 Koeberl C. (1992) Geochemistry and origin of Muong Nong-type tektites. *Geochim. Cosmochim. Acta* **56**, 1033–
976 1064.
977 Koeberl C. (1986) Geochemistry of Tektites and Impact Glasses. *Annu. Rev. Earth Planet. Sci.* **14**, 323–350.
978 Koeberl C. (1988) The origin of tektites: a geochemical discussion. *Proc. NIPR Symp. Antarct. Meteor.* **1**, 261–290.

Koeberl C., Kluger F. and Kiesl W. (1984) Geochemistry of Muong-Nong type tektites: IV. Selected trace element correlations. *J. Geophys. Res. Solid Earth* **89**, C351–C357.
Landron C., Hennet L., Coutures J.-P., Jenkins T., Alétru C., Greaves N., Soper A. and Derbyshire G. (2000) Aerodynamic laser-heated contactless furnace for neutron scattering experiments at elevated temperatures. *Rev. Sci. Instrum.* **71**, 1745–1751.
Li W., Jackson S. E., Pearson N. J., Alard O. and Chappell B. W. (2009) The Cu isotopic signature of granites from the Lachlan Fold Belt, SE Australia. *Chem. Geol.* **258**, 38–49.
Liu S.-A., Huang J., Liu J., Wörner G., Yang W., Tang Y.-J., Chen Y., Tang L., Zheng J. and Li S. (2015) Copper isotopic composition of the silicate Earth. *Earth Planet. Sci. Lett.* **427**, 95–103.
Liu S.-A., Li D., Li S., Teng F.-Z., Ke S., He Y. and Lu Y. (2014) High-precision copper and iron isotope analysis of igneous rock standards by MC-ICP-MS. *J. Anal. At. Spectrom.* **29**, 122–133.
Lodders K. (2003) Solar System Abundances and Condensation Temperatures of the Elements. *Astrophys. J.* **591**, 1220.
Macris C. A., Asimow P. D., Badro J., Eiler J. M., Zhang Y. and Stolper E. M. (2018) Seconds after impact: Insights into the thermal history of impact ejecta from diffusion between lechatelierite and host glass in tektites and experiments. *Geochim. Cosmochim. Acta* **241**, 69–94.
Magna T., Deutsch A., Mezger K., Skála R., Seitz H.-M., Mizera J., Řanda Z. and Adolph L. (2011) Lithium in tektites and impact glasses: Implications for sources, histories and large impacts. *Geochim. Cosmochim. Acta* **75**, 2137–2158.
Maréchal C. N., Télouk P. and Albarède F. (1999) Precise analysis of copper and zinc isotopic compositions by plasma-source mass spectrometry. *Chem. Geol.* **156**, 251–273.
McDonough W. F. and Sun S. -s. (1995) The composition of the Earth. *Chem. Geol.* **120**, 223–253.
Melosh H. J. (1989) *Impact cratering: A geologic process*., New York, Oxford University Press. Available at: http://adsabs.harvard.edu/abs/1989icgp.book.....M [Accessed October 4, 2019].
Melosh H. J. and Artemieva N. (2004) How Does Tektite Glass Lose Its Water? *Lunar Planet. Sci. Conf.* **35**. Available at: http://adsabs.harvard.edu/abs/2004LPI....35.1723M [Accessed December 23, 2019].
Moeller K., Schoenberg R., Pedersen R.-B., Weiss D. and Dong S. (2012) Calibration of the New Certified Reference Materials ERM-AE633 and ERM-AE647 for Copper and IRMM-3702 for Zinc Isotope Amount Ratio Determinations. *Geostand. Geoanalytical Res.* **36**, 177–199.
Moynier F., Albarède F. and Herzog G. F. (2006) Isotopic composition of zinc, copper, and iron in lunar samples. *Geochim. Cosmochim. Acta* **70**, 6103–6117.
Moynier F., Beck P., Jourdan F., Yin Q.-Z., Reimold U. and Koeberl C. (2009) Isotopic fractionation of zinc in tektites. *Earth Planet. Sci. Lett.* **277**, 482–489.
Moynier F., Koeberl C., Beck P., Jourdan F. and Telouk P. (2010) Isotopic fractionation of Cu in tektites. *Geochim. Cosmochim. Acta* **74**, 799–807.
Moynier F., Vance D., Fujii T. and Savage P. (2017) The Isotope Geochemistry of Zinc and Copper. *Rev. Mineral. Geochem.* **82**, 543–600.
Ni H., Shi H., Zhang L., Li W.-C., Guo X. and Liang T. (2018) Cu diffusivity in granitic melts with application to the formation of porphyry Cu deposits. *Contrib. Mineral. Petrol.* **173**, 50.
Ni P. and Zhang Y. (2016) Cu diffusion in a basaltic melt. *Am. Mineral.* **101**, 1474–1482.
Ni P., Zhang Y., Chen S. and Gagnon J. (2019) A melt inclusion study on volatile abundances in the lunar mantle. *Geochim. Cosmochim. Acta* **249**, 17–41.
Ni P., Zhang Y., Simon A. and Gagnon J. (2017) Cu and Fe diffusion in rhyolitic melts during chalcocite "dissolution": Implications for porphyry ore deposits and tektites. *Am. Mineral.* **102**, 1287–1301.
Nie N. X. and Dauphas N. (2019) Vapor Drainage in the Protolunar Disk as the Cause for the Depletion in Volatile Elements of the Moon. *Astrophys. J.* **884**, L48.
Norris C. A. and Wood B. J. (2017) Earth's volatile contents established by melting and vaporization. *Nature* **549**, 507–510.
Pack A., Kremer K., Albrecht N., Simon K. and Kronz A. (2010) Description of an aerodynamic levitation apparatus with applications in Earth sciences. *Geochem. Trans.* **11**, 4.
Richter F. M., Dauphas N. and Teng F.-Z. (2009) Non-traditional fractionation of non-traditional isotopes: Evaporation, chemical diffusion and Soret diffusion. *Chem. Geol.* **258**, 92–103.
Richter F. M., Davis A. M., Ebel D. S. and Hashimoto A. (2002) Elemental and isotopic fractionation of Type B calcium-, aluminum-rich inclusions: experiments, theoretical considerations, and constraints on their thermal evolution. *Geochim. Cosmochim. Acta* **66**, 521–540.

1034 Richter F. M., Janney P. E., Mendybaev R. A., Davis A. M. and Wadhwa M. (2007) Elemental and isotopic
1035 fractionation of Type B CAI-like liquids by evaporation. *Geochim. Cosmochim. Acta* **71**, 5544–5564.
1036 Ripley E. M. and Brophy J. G. (1995) Solubility of copper in a sulfur-free mafic melt. *Geochim. Cosmochim. Acta*
1037 **59**, 5027–5030.
1038 Rodovská Z., Magna T., Žák K., Kato C., Savage P. S., Moynier F., Skála R. and Ježek J. (2017) Implications for
1039 behavior of volatile elements during impacts—Zinc and copper systematics in sediments from the Ries impact
1040 structure and central European tektites. *Meteorit. Planet. Sci.* **52**, 2178–2192.
1041 Rodovská Z., Magna T., Žák K., Skála R., Brachaniec T. and Visscher C. (2016) The fate of moderately volatile
1042 elements in impact events—Lithium connection between the Ries sediments and central European tektites.
1043 *Meteorit. Planet. Sci.* **51**, 2403–2415.
1044 Rudnick R. L. and Gao S. (2003) 3.01 - Composition of the Continental Crust. In *Treatise on Geochemistry* (eds. H.
1045 D. Holland and K. K. Turekian). Pergamon, Oxford. pp. 1–64. Available at:
1046 http://www.sciencedirect.com/science/article/pii/B0080437516030164 [Accessed September 26, 2018].
1047 Savage P. S., Moynier F., Chen H., Shofner G., Siebert J., Badro J. and Puchtel I. S. (2015) Copper isotope evidence
1048 for large-scale sulphide fractionation during Earth's differentiation. *Geochem. Perspect. Lett.* Available at:
1049 https://research-repository.st-andrews.ac.uk/handle/10023/6803 [Accessed October 16, 2017].
1050 Shields W. R., Goldich S. S., Garner E. L. and Murphy T. J. (1995) Natural variations in the abundance ratio and the
1051 atomic weight of copper. *J. Geophys. Res.* **70**, 479–491.
1052 Sossi P. A., Halverson G. P., Nebel O. and Eggins S. M. (2015) Combined Separation of Cu, Fe and Zn from Rock
1053 Matrices and Improved Analytical Protocols for Stable Isotope Determination. *Geostand. Geoanalytical Res.* **39**,
1054 129–149.
1055 Sossi P. A., Klemme S., O'Neill H. St. C., Berndt J. and Moynier F. (2019) Evaporation of moderately volatile
1056 elements from silicate melts: experiments and theory. *Geochim. Cosmochim. Acta* **260**, 204–231.
1057 Stöffler D., Artemieva N. A. and Pierazzo E. (2002) Modeling the Ries-Steinheim impact event and the formation of
1058 the moldavite strewn field. *Meteorit. Planet. Sci.* **37**, 1893–1907.
1059 Urey H. C. (1947) The thermodynamic properties of isotopic substances. *J. Chem. Soc. Resumed* **0**, 562–581.
1060 Wang K. and Jacobsen S. B. (2016) Potassium isotopic evidence for a high-energy giant impact origin of the Moon.
1061 *Nature* **538**, 487–490.
1062 Weber R. J. K., Felten J. J. and Nordine P. C. (1996) Laser hearth melt processing of ceramic materials. *Rev. Sci.*
1063 *Instrum.* **67**, 522–524.
1064 Wimpenny J., Marks N., Knight K., Rolison J. M., Borg L., Eppich G., Badro J., Ryerson F. J., Sanborn M.,
1065 Huyskens M. H. and Yin Q. (2019) Experimental determination of Zn isotope fractionation during evaporative
1066 loss at extreme temperatures. *Geochim. Cosmochim. Acta* **259**, 391–411.
1067 Wombacher F., Rehkämper M., Mezger K. and Münker C. (2003) Stable isotope compositions of cadmium in
1068 geological materials and meteorites determined by multiple-collector ICPMS. *Geochim. Cosmochim. Acta* **67**,
1069 4639–4654.
1070 Xia Y., Kiseeva E., Wade J. and Huang F. (2019) The effect of core segregation on the Cu and Zn isotope
1071 composition of the silicate Moon. *Geochem. Perspect. Lett.* Available at:
1072 https://ora.ox.ac.uk/objects/uuid:f7736bd6-af8b-4a69-bbb4-8d5e16788230 [Accessed November 19, 2019].
1073 Yang Y., Zhang Y., Simon A. and Ni P. (2016) Cassiterite dissolution and Sn diffusion in silicate melts of variable
1074 water content. *Chem. Geol.* **441**, 162–176.
1075 Yu Y., Hewins R. H., Alexander C. M. O. 'D. and Wang J. (2003) Experimental study of evaporation and isotopic
1076 mass fractionation of potassium in silicate melts. *Geochim. Cosmochim. Acta* **67**, 773–786.
1077 Zajacz Z., Candela P. A., Piccoli P. M., Sanchez-Valle C. and Wälle M. (2013) Solubility and partitioning behavior
1078 of Au, Cu, Ag and reduced S in magmas. *Geochim. Cosmochim. Acta* **112**, 288–304.
1079 Žák K., Skála R., Řanda Z., Mizera J., Heissig K., Ackerman L., Ďurišová J., Jonášová Š., Kameník J. and Magna T.
1080 (2016) Chemistry of Tertiary sediments in the surroundings of the Ries impact structure and moldavite formation
1081 revisited. *Geochim. Cosmochim. Acta* **179**, 287–311.
1082 Zhang Y. (2008) *Geochemical Kinetics*., Princeton University Press.
1083